



Contents lists available at ScienceDirect

Arabian Journal of Chemistry

journal homepage: www.ksu.edu.sa

Optimizing sponge-like activated carbon from *Manihot esculenta* tubers for high-performance supercapacitors

Markus Diantoro^{a,*}, Nuviya Illa Muthi Aturroifah^a, Joko Utomo^a, Ishmah Luthfiyah^{a,e}, Ida Hamidah^b, Brian Yulianto^c, Andrivo Rusydi^d, Worawat Meevesana^e, Santi Maensiri^e, Pramod K. Singh^f

^a Department of Physics, Faculty of Mathematics and Natural Sciences, Universitas Negeri Malang, Jl. Semarang 5, Malang 65145, Indonesia

^b Department of Engineering and Vocational Education, Universitas Pendidikan Indonesia, Jl. Dr. Setiabudhi 207, Bandung 40154, Indonesia

^c Advanced Functional Materials Laboratory, Department of Engineering Physics, Institute of Technology Bandung (ITB), Bandung 40132, Indonesia

^d Singapore Synchrotron Light Source, National University of Singapore, 5 Research Link, Singapore 117603, Singapore

^e School of Physics Faculty of Science, Suranaree University of Technology, Nakhon Ratchasima, Thailand

^f Center for Solar Cells & Renewable Energy, Department of Physics, Sharda University, Greater Noida 201310, India

ARTICLE INFO

Keywords:

Sponge-like activated carbon

Waste biomass

Manihot esculenta tubers

KOH activation

Supercapacitor

ABSTRACT

Activated carbon plays a crucial role in enhancing supercapacitor performance by optimizing parameters such as surface area, pore structure, and morphology. This study investigates activated carbon derived from *Manihot esculenta* tubers, which offers a promising, sponge-like porous morphology suitable for supercapacitor electrodes. Activated carbon derived from *Manihot esculenta* tubers was synthesized utilizing chemical activation with varying concentrations of potassium hydroxide (KOH) as the activator 0 M (C-S0), 1 M (AC-S1M), 2 M (AC-S2M), and 4 M (AC-S4M). The AC-S4M sample variant achieved the highest surface area ($471.645 \text{ m}^2\text{g}^{-1}$) and total volume ($0.253 \text{ cm}^3\text{g}^{-1}$). Electrochemical characterization using symmetric coin cell supercapacitors demonstrated excellent specific capacitance of 146.570 Fg^{-1} at 0.1 Ag^{-1} in a 6 M KOH aqueous electrolyte. Notably, the highest energy density of 15.525 Whkg^{-1} at a power density of 174.660 Wkg^{-1} was achieved. These results underscore the potential of *Manihot esculenta* tubers-derived activated carbon as a sustainable, high-performance electrode material, advancing environmentally friendly energy storage technologies, which remain interesting for further studies.

1. Introduction

Supercapacitors are innovative technologies developed as energy storage devices that surpass conventional capacitors. According to Market Research Consulting, the demand for supercapacitors in the global market will continue to increase from 2019 to 2030 (Lasrado et al., 2021). The advantages of supercapacitors as energy storage devices include high power density ($2\text{--}5 \text{ kWkg}^{-1}$), high stability, fast recharge time, and long cycle life (Baig and Gul, 2021; Kalu-Uka et al., 2022). The limited energy density of supercapacitors hinders their

widespread adoption in electric vehicles and electronic devices. Thus, efforts must be made to raise energy density to preserve the cycle life and performance of power densities. Increased specific capacitance leads to increased energy density.

One effective strategy to improve the electrochemical performance of supercapacitors is to use active electrode materials with high electrical conductivity and large surface area (Borenstein et al., 2017). Various active materials that are often used for supercapacitor electrodes include metal oxides, metal-organic frameworks (MOFs), covalent-organic frameworks (COFs), conductive polymers, and

Abbreviations: Co, Company; USA, United States of America; MA, Massachusetts; LIB, Lithium-ion battery; Ltd, Limited; C-S0, *Manihot esculenta* tubers-carbon before KOH activation; AC-S1M, *Manihot esculenta* tubers-activated carbon resulting from activation using 1 M KOH concentration; AC-S2M, *Manihot esculenta* tubers-activated carbon resulting from activation using 2 M KOH concentration; AC-S4M, *Manihot esculenta* tubers-activated carbon resulting from activation using 4 M KOH concentration.

* Corresponding author at: Department of Physics, Faculty of Mathematics and Natural Sciences, Universitas Negeri Malang, Jl. Semarang 5, Malang 65145, Indonesia.

E-mail address: markus.diantoro.fmipa@um.ac.id (M. Diantoro).

<https://doi.org/10.1016/j.arabjc.2024.106068>

Received 14 August 2024; Accepted 19 November 2024

Available online 28 November 2024

1878-5352/© 2024 The Author(s). Published by Elsevier B.V. on behalf of King Saud University. This is an open access article under the CC BY-NC-ND license (<http://creativecommons.org/licenses/by-nc-nd/4.0/>).

activated carbon (Adoor et al., 2024; Adoor et al., 2023; Agadi et al., 2024; Pramitha et al., 2024; Pramitha et al., 2023). Compared with other materials, such as metal oxides (such as Mn_3O_4 and Co_3O_4), MOFs, COFs, and conductive polymers, activated carbon offers a wider pore size range that supports ion accommodation and enables efficient ion diffusion. The interconnected pore structure further contributes to substantial energy storage capacity and superior energy and power densities. In activated carbon-based electric double-layer capacitors (EDLCs), charging is initiated by depositing negative and positive electrolyte ions on the cathode and anode under an applied voltage (Intan Subadra et al., 2019). During discharge, the ions become randomly oriented, and the electrodes are left uncharged. The electrochemical performance of EDLC is greatly influenced by the raw material of activated carbon, activated carbon derived from biomass materials has the advantages of being abundantly available, cost-effective, and easy to synthesize (Ghosh et al., 2019).

Based on data from 2014 to 2018, the demand for imported activated carbon in Indonesia reached 10,630 tons per year, with a compound annual growth rate of 1.5 %. Import activities were necessary to fulfill the demand for activated carbon in Indonesia, as local sources proved inadequate. Based on President Decree No. 29 of 2018, regulations regarding industrial empowerment were issued. The President Decree mandates using local content at a rate of more than 40 %. Local natural resources in Indonesia are widely utilized as sources for activated carbon production (Adinaveen et al., 2013).

The synthesis of activated carbon is influenced by various parameters, including the activation method, activating agent, synthesis procedure, and raw material (Thongpat et al., 2021). Physical activation and chemical activation are two frequent activation techniques. Physical activation involves thermal treatment of the material in the presence of oxidizing or inert gases such as carbon dioxide (CO_2), nitrogen (N_2), or argon (Ar), resulting in pore formation (Illingworth et al., 2022). One disadvantage of physical activation is that high temperatures can lead to increased ash content and reduced carbon content in certain biomass materials. In contrast, chemical activation is a process that utilizes chemicals including potassium hydroxide, sodium hydroxide, phosphoric acid, sulfuric acid, and zinc chloride as activating agents (Chen et al., 2012; Demir and Doguscu, 2022; He et al., 2013).

Supercapacitor electrodes typically use activated carbon precursors derived from biomass materials such as coconut shells, bagasse, straw, bamboo, coffee, and cassava, which have been proven effective in enhancing electrode performance (Charoensook et al., 2021a; Omokafe, 2020; Zhang et al., 2018). However, certain limitations remain, such as the need for higher specific capacitance as well as improved surface area and pore volume for large-scale applications. This study aims to address these limitations by exploring the underutilized potential of *Manihot esculenta* (cassava) to produce highly porous activated carbon through controlled chemical activation. According to data from the Food and Agriculture Organization from 2012 to 2022, Indonesia ranks 6th globally in *Manihot esculenta* production, with a cultivation area covering approximately 19,155,594 ha. *Manihot esculenta* is commonly used in food and tapioca flour production. *Manihot esculenta* also has the potential for use in non-food products, particularly in energy storage materials. Nevertheless, the potential has not yet been fully realized. *Manihot esculenta* has a high content of lignin (13.42 %), cellulose (39.29 %), and hemicellulose (24.34 %) (Lismeri et al., 2021). The composition contributes to the significant porosity and surface area of the resulting activated carbon. Previous research on *Manihot esculenta*-derived activated carbon has shown promising results in terms of surface area and porosity, particularly when activated using ZnCl_2 ($1567 \text{ m}^2\text{g}^{-1}$, $0.54 \text{ cm}^3\text{g}^{-1}$), KOH ($1605 \text{ m}^2\text{g}^{-1}$, $0.691 \text{ cm}^3\text{g}^{-1}$), and H_2SO_4 ($398.46 \text{ m}^2\text{g}^{-1}$, $0.1639 \text{ cm}^3\text{g}^{-1}$) (Ospino Orozco et al., 2022; Shrestha, 2022; Zhang et al., 2018). Furthermore, the activated carbon derived from *Manihot esculenta* exhibits a porous morphology with a surface area of $1350 \text{ m}^2\text{g}^{-1}$, which enhances ion transport and electrolyte accessibility (Chaisit et al., 2020). Based on previous studies, the synthesis of

activated carbon from various parts of *Manihot esculenta*, including stems, peels, roots, and starch, the potential of tubers as a carbon source is still unexplored. Furthermore, previous studies, such as the work of Chaisit et al., only used one concentration of KOH during activation. In this study, we systematically vary the concentration of KOH to improve the electrochemical properties of activated carbon derived from *Manihot esculenta* tubers, providing insight into its potential for high-performance energy storage applications. This study improves current knowledge by examining the effects of various concentrations of KOH (0, 1, 2, and 4 M) on the activation of *Manihot esculenta* tubers to produce activated carbon with porous morphology and higher specific capacitance for supercapacitor electrodes. The previous results show that using KOH not only enhances the porosity but also increases the specific capacitance to 179 Fg^{-1} , which is better than the previous results with Na_2SO_4 (80 Fg^{-1}) and H_2SO_4 (64 Fg^{-1}) (Chaisit et al., 2020; Ospino Orozco et al., 2022). By optimizing the KOH concentration, this research offers a more effective and scalable method for producing high-performance supercapacitor electrodes.

2. Materials and methods

2.1. Materials

Waste *Manihot esculenta* was procured from a traditional market in Malang, Indonesia. All chemicals employed in this study were of analytical purity and used without further refinement: potassium hydroxide (KOH, Sigma Aldrich Chemical Reagent Co., USA), hydrochloric acid (HCl, Sigma Aldrich Chemical Reagent Co., USA), N-methyl-2-pyrrolidone (NMP, Sigma Aldrich, Burlington, MA, USA), polyvinylidene fluoride (PVDF, Dongguan Gelon LIB Co., Ltd., China), and carbon black (CB, Imerys, La Hulpe, Belgium) as a conductive additive. Nickel foam served as the substrate, and coin-type cells were obtained from TOB Machine, Fujian, China.

2.2. Activated carbon synthesis

As shown in Fig. 1, the *Manihot esculenta* was subjected to chemical activation. The initial step in this process was peeling the *Manihot esculenta* to remove the peel from the tubers. In this study, the tubers of *Manihot esculenta* were used. Then, the *Manihot esculenta* tubers were cut into ± 3 cm in size and dried under the sun for 12 h to remove excess moisture. The dried *Manihot esculenta* tubers were pre-carbonated at 400°C for 2 h until they turned carbon. Next, the carbonized *Manihot esculenta* tubers were pulverized and passed through a 200-mesh sieve to achieve a uniform particle size. The *Manihot esculenta* tubers carbon was mixed in 50 mL of KOH solution with concentrations of 0 M, 1 M, 2 M, and 4 M (called C-S0, AC-S1M, AC-S2M, and AC-S4M) and stirred for 24 h at room temperature. The washing process was carried out in 2 stages, the first washing using 1 M HCl, then continued using distilled water until it reached a neutral pH. The activated carbon was desiccated in an oven at 110°C for 24 h, followed by calcination in a furnace at 600°C for 60 min.

2.3. Electrode preparation and fabrication of EDLC coin cell

The electrodes were fabricated by mixing activated carbon derived from *Manihot esculenta* tubers as the active material, carbon black (CB), and PVDF in a weight ratio of 8:1:1. The total mass of the electrode was 1 g, with 0.8 g consisting of the active material. The resulting slurry was homogenized through 12 h of continuous stirring. The nickel foam substrate was cut into the form of a disc with a diameter of 1.5 cm. The nickel foam substrate was coated on both sides with $20 \mu\text{L}$ of *Manihot esculenta* tubers-based electrode paste using a micropipette. The electrodes were heated in an oven at 80°C for 1 h. *Manihot esculenta* activated carbon electrodes were pressed with a load of 500 kg to produce thin film electrodes. Finally, the electrodes were immersed in 5 mL of 6

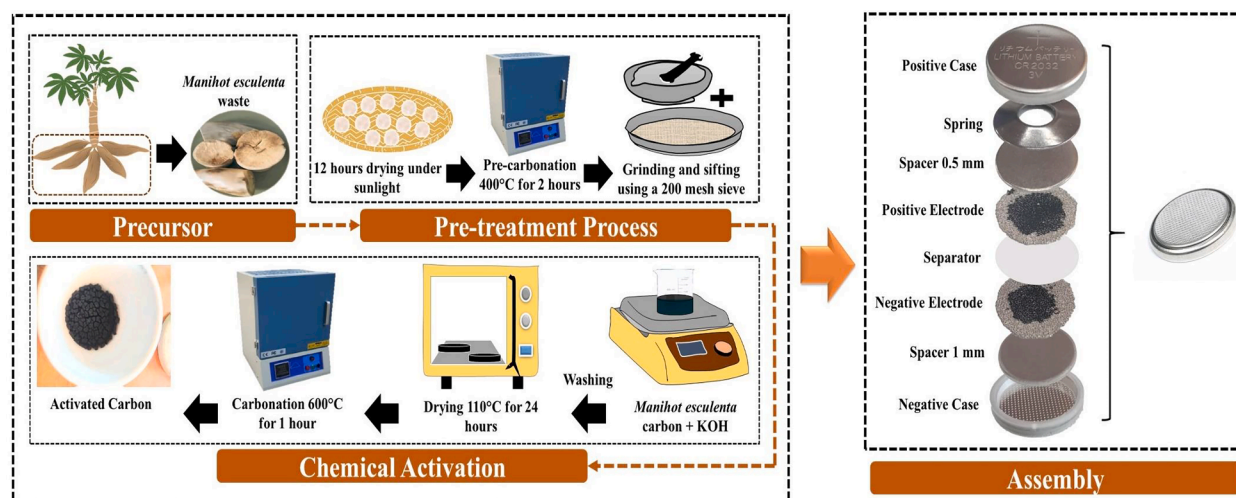


Fig. 1. Synthesis schematic illustration and EDLC coin cell assembly of *Manihot esculenta* tubers-activated carbon.

M KOH solution electrolyte for 24 h. The electrodes were arranged using a coin cell, with the arrangement as shown in Fig. 1.

2.4. Materials characterization

The microstructure of the activated carbon was examined through scanning electron microscopy (SEM), Brunauer-Emmett-Teller (BET) analysis, X-ray diffraction (XRD), Raman spectroscopy, Fourier transform infrared (FTIR), and X-ray photoelectron spectroscopy (XPS). SEM with the brand FEI Inspect-S50 type was used to determine the pore structure of the activated carbon of *Manihot esculenta* tubers. The N_2 adsorption analyzer utilizes the Brunauer-Emmett-Teller (BET) method using Tristar II Plus 3020. The micropore volume (V_{micro}) and external surface area (S_{ext}) from the N_2 adsorption were determined by t-plot using the De Boer method in Eq. (1) (De Boer, 1965),

$$t(\text{\AA}) = \left[\frac{13.99}{0.034 - \log\left(\frac{P}{P_0}\right)} \right]^{0.5} \quad (1)$$

where P/P_0 is the relative pressure. Based on the t-plot graph, the relationship between statistical thickness (t ; nm) and adsorbed quantity (cm^3g^{-1} STP) produces a straight line with intercept (i) and slope (s) which is used to determine micropore volume (V_{micro}) and external surface area (S_{ext}) as in Eqs. (2) and (3) (Tran et al., 2018),

$$V_{micro}(\text{cm}^3\text{g}^{-1}) = 0.001547 \times i \quad (2)$$

$$S_{ext}(\text{m}^2\text{g}^{-1}) = 15.47 \times s \quad (3)$$

The constant 15.47 denotes the conversion factor from gas to liquid volume. The crystallinity and diffraction pattern of the *Manihot esculenta* tubers-based activated carbon were characterized using X-ray diffraction. The PANalytical 4 instrument was operated at 2θ ranging 10–90 °C using $\text{CuK}\alpha$ radiation sources ($\lambda = 0.15406$ nm). Raman spectroscopy was employed to conduct a more comprehensive chemical composition analysis. FTIR analysis was conducted on the activated carbon using a Shimadzu IR Prestige 21 spectrophotometer to identify functional groups. The operating spectrum range is 400 cm^{-1} to 4000 cm^{-1} in transmission mode with a resolution of 4 cm^{-1} . X-ray photoelectron spectroscopy (XPS PHI5000 Versa Probe II, ULVAC-PHI, Japan) was employed to analyse the elemental composition.

2.5. Electrochemical measurements

Electrochemical properties of the coin cell supercapacitor were evaluated using galvanostatic charge–discharge (GCD), cyclic voltammetry (CV), and electrochemical impedance spectroscopy (EIS). GCD measurements were performed on a NEWARE Battery Testing System, while CV and EIS were conducted using a Palmsens4 potentiostat. EIS measurements use a frequency range of 0.01 to 100 kHz. The charge–discharge cycle was measured at a current density of 0.1 Ag^{-1} and a cut-off voltage of 0.0–1.0 V. Specific capacitance was determined from the discharge current (I), discharge time (t), electrode mass (m), and potential difference (ΔV) using Eq. (4) (Zapata Benabithé et al., 2013),

$$C_s(\text{Fg}^{-1}) = \frac{4 \times I \times t}{m \times \Delta V} \quad (4)$$

The energy density (ED) and power density (PD) were calculated according to Eqs. (5) and (6) (Saputro et al., 2020; Yang and Park, 2020),

$$ED(\text{Whkg}^{-1}) = \frac{0.5 \times C_s \times (\Delta V)^2}{3.6} \quad (5)$$

$$EP(\text{Wkg}^{-1}) = \frac{3600 \times ED}{t} \quad (6)$$

3. Results and discussion

3.1. Morphological and microstructure analysis

SEM images of activated carbon from *Manihot esculenta* tubers before and after activation are shown in Fig. 2(a–d). SEM image with low magnification ($800\times$) shows that increasing the KOH concentration in the activation process produces increasingly smaller activated carbon particles from *Manihot esculenta* tubers. KOH plays a role in the process of breaking down larger carbon particles into smaller and more uniform structures, thereby increasing the efficiency and performance of electrical energy storage (Chaudhary et al., 2024).

Fig. 2(e–h) depict the porosity morphology of activated carbon derived from *Manihot esculenta* tubers. The surface morphology reveals a porous and smooth structure, which varies with the concentration of the KOH activator. The KOH activator plays a role in the formation of sponge-shaped pores in the activated carbon derived from *Manihot esculenta* tubers. Morphological analysis indicates that pore diameter decreases with increasing KOH concentration. Fig. 2(e) shows that pre-activated *Manihot esculenta* tubers have pores with larger diameters. Fig. 2(f–h) show that post-activation with KOH, activated carbon pores

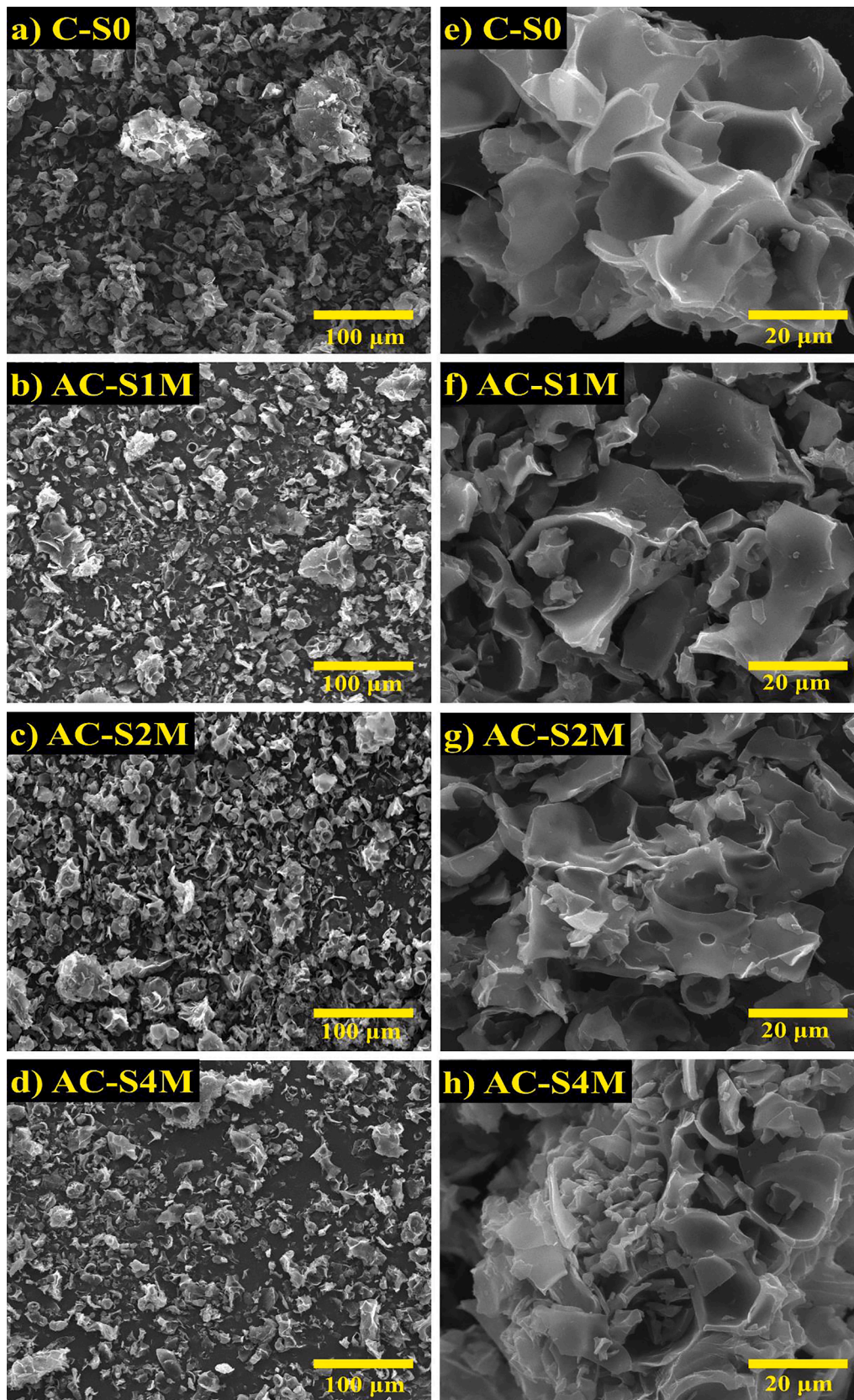


Fig. 2. SEM images magnification 800 \times (a-d) and 5000 \times (e-h) of *Manihot esculenta* tubers-activated carbon on the variation of KOH activator.

increase, and the pore diameter decreases. The sponge-like pore structure facilitates rapid ion transport within the electrode, leading to enhanced electrochemical properties in supercapacitors (Wu et al., 2025). The pore structure of activated carbon significantly impacts the accessibility of ions to the electrode surface. The pore structure of activated carbon derived from *Manihot esculenta* tubers is open and directly connected to the electrode surface, facilitating faster ion mobility. Table 1 presents the characteristics of the activated carbon derived from *Manihot esculenta* tubers, including particle dimensions, pore size, and porosity percentage. Variations in dimensions and pore size can lead to differences in porosity, which consequently can affect the electrical performance (Atchudan et al., 2022).

Table 1 shows that particle size and pore diameter decrease, but the porosity percentage increases with increasing KOH activator concentration. According to research conducted by (Chaisit et al., 2020), particle size affects the decrease of the surface area. The role of KOH in the activation process is to oxidize and erode other materials in the carbon. The KOH activator also breaks bond chains to reduce particle size and increase porosity. The smaller particle size distribution results in smaller and more numerous pores, enhancing supercapacitor performance. The reduced particle size and increased pores signify high electrochemical performance and capacitance, attributed to the enhanced capacity for accommodating electrolyte ions within the pores and improved electrolyte ion diffusion.

Pore structures of *Manihot esculenta* tubers-activated carbon were contrasted and analysed to further explore their physical properties. Adsorption and desorption isotherm analysis of N₂ was carried out through BET characterization, aiming to analyse *Manihot esculenta* tubers-activated carbon pore properties and specific surface area. BET analysis on *Manihot esculenta* tubers-activated carbon is presented in Fig. 3(a–d). Based on Fig. 3(a), a linear graph of isotherms shows that *Manihot esculenta* tubers-activated carbon corresponds to the type I isotherm ($P/P_0 < 0.3$) according to the IUPAC classification (Rawal et al., 2018). The graph begins with the sharp increase caused by the absorption process of the main nitrogen gas. A sharp increase at $P/P_0 < 0.3$ indicates the sample has microporous-sized particles with a small external surface area. A steady increase after the initial rise indicates the presence of mesoporous and macropore-sized particles. The adsorption and desorption of N₂ on the samples yielded overlapping graphs, signifying the presence of numerous microporous-sized particles. Mesopore analysis is depicted in the BJH pore size distribution, which shows that *Manihot esculenta* tubers-activated carbon has a pore diameter range of 1.9–3.8 nm, as illustrated in Fig. 3(b). Based on research by M. Vinayagam et al., the findings indicate the existence of micropores in the samples (Vinayagam et al., 2024b). The t-plot for the *Manihot esculenta* activated carbon was constructed within the relative pressure range of 0.05 to 0.35. Micropore volume and external surface area were subsequently determined from the t-plot intercept and slope, respectively, using Eqs. (2) and (3) (Fig. 3(c)).

Table 2 reveals that the AC-S4M sample possesses the highest micropore surface area ($376.382 \text{ m}^2\text{g}^{-1}$), external surface area ($95.263 \text{ m}^2\text{g}^{-1}$), and total BET surface area ($471.645 \text{ m}^2\text{g}^{-1}$), along with a micropore volume of $0.185 \text{ cm}^3\text{g}^{-1}$. According to Fig. 3(d), *Manihot esculenta* tubers-activated carbon exhibits a higher micropore volume than mesopore and macropore volumes. Microporous-sized particles are very good at increasing the ability to store electrochemical energy

Table 1
Particle size, pore diameter, and porosity percentage of *Manihot esculenta* tuber-activated carbon.

Sample	Particle Size (μm)	Pore Diameter (μm)	% of Porosity
C-S0	12.371	4.069	64.158
AC-S1M	8.905	3.422	73.542
AC-S2M	5.811	2.184	74.456
AC-S4M	5.480	1.789	74.918

(Supawet Phainuphong et al., 2022). The BET surface area of activated carbons derived from *Manihot esculenta* tubers was determined for various activator concentrations and is presented in Table 2. The C-S0 sample has the lowest surface area of $413,794 \text{ m}^2\text{g}^{-1}$. The activation process significantly increases the surface area of the samples. Specifically, surface areas of 418.695, 449.417, and $471.645 \text{ m}^2\text{g}^{-1}$ were achieved for AC-1 M, AC-2 M, and AC-4 M, respectively. The larger surface area can increase the charge storage capacity for energy applications.

The diffraction pattern using XRD from *Manihot esculenta* tubers-activated carbon and Thailand commercial activated carbon is presented in Fig. 4(a) to analyse the phase and crystallinity of the activated carbon of *Manihot esculenta* tubers. The diffraction of *Manihot esculenta* tubers-activated carbon is marked as pre-activation (C-S0), post-chemical activation (AC-S1M, AC-S2M, AC-S4M), and commercial activated carbon (AC-Commercial). X-ray diffraction patterns of activated carbon prepared from *Manihot esculenta* tubers reveal characteristic peaks at $2\theta = 23^\circ$ (002) and 43° (100). The presence of an amorphous phase, along with a well-defined peak at $2\theta = 23^\circ$ indicative of a graphitic structure, is supported by the diffraction pattern (Yang et al., 2020). The amorphous phase of *Manihot esculenta* tubers-activated carbon adopts a turbostratic model, signifying a graphite-like layer with microscopic defects and irregularities, and includes two diffraction peaks within the graphite peaks on a flat plane (planar). Based on the XRD diffraction pattern, the first diffraction peak with a large area is produced at $2\theta = 19.58^\circ$ (C-S0), 23.77° (AC-S1M), 23.56° (AC-S2M), 23.56° (AC-S4M), and 23.56° (AC-Commercial). The first peak in the C-S0 sample is not located in the same place as the other samples. The KOH is indicated to be responsible for rearranging the carbon atoms to their correct location (Farma et al., 2021b; Latupeirissa et al., 2016). The second peak is at $2\theta = 43.33^\circ$ (AC-S1M), 42.75° (AC-S2M), 42.75° (AC-S4M), and 43.29° (AC-Commercial), with an area smaller than the first peak. The low peak intensity in the C-S0 sample is due to the lack of chemical activation and high-temperature carbonation, where final carbonation leads to the rearrangement of carbon, forming more carbon-intensive materials. In AC-S1M and AC-S2M samples, the low intensity of the second peak indicates incomplete formation of activated carbon. The AC-S4M sample shows the highest diffraction peak intensity, and the intensity increases with higher KOH concentration, revealing the formation of a hexagonal crystal structure from cellulose content. The increase in KOH activator concentration is directly related to the smaller particle size. The chemical activation process of carbon-based *Manihot esculenta* tubers produces a diffraction pattern similar to that of commercial activated carbon.

The activated carbon structure of *Manihot esculenta* tubers is more explicitly understood through Raman characterization. Raman characterization is a sensitive method used to detect abnormalities in carbon materials at the molecular level and analyze the chemical bonds responsible for resonance in the Raman spectrum. Based on Fig. 4(b–d), four peaks (I, D, D', G band) are observed in the Raman characterization of *Manihot esculenta* tubers-activated carbon. As demonstrated in the study by Chen, Weimin, et al. and Yin, Yanshan, et al., the fitting process was applied to the four peaks obtained in our research (Chen et al., 2017; Yadav et al., 2022; Yin et al., 2018). The peaks are the D band ($1300\text{--}1400 \text{ cm}^{-1}$) and the G band ($1500\text{--}1600 \text{ cm}^{-1}$). Based on Table 3, the I band at 1233.943 cm^{-1} (C-S0) and 1250.392 cm^{-1} (AC-S4M) indicate the presence of impurities in the structure of graphite. The D band represents a defect carbon that has a lower intensity than the G band (Ahmed et al., 2018; Yumak et al., 2019). The D band is related to the charge storage capacity of *Manihot esculenta* tubers-activated carbon, indicating the interaction between graphite carbon atoms and electrolyte ions (Sahoo and Rao, 2021). The D' band observed at 1446.767 cm^{-1} (C-S0) and 1512.185 cm^{-1} (AC-S4M) is associated with amorphous sp²-bonded carbon fragments or functional groups within the disordered structure. The bands located at 1446.767 cm^{-1} (C-S0) and 1512.185 cm^{-1} (AC-S4M) suggest irregularities in the stacking sequence

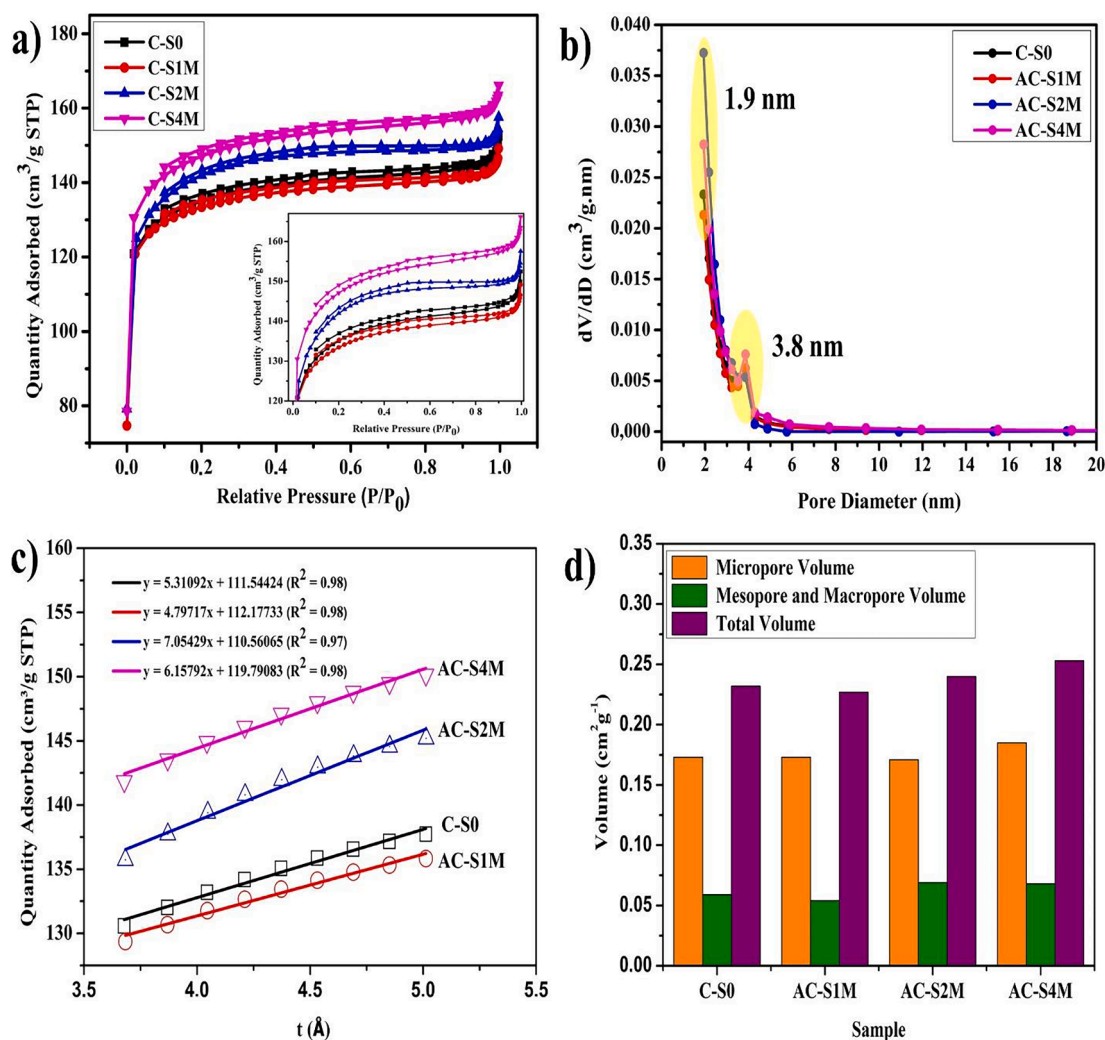


Fig. 3. (a) BET isotherm plot, (b) BJH pore diameter distribution, (c) t-plot graph, (d) pore volume distribution of *Manihot esculenta* tubers-activated carbon at various concentrations of KOH activator.

Table 2

BET analysis of *Manihot esculenta* tuber-activated carbon at various concentrations of KOH activator (0, 1, 2, 4 M).

Sample	BET SSA (m^2g^{-1})			$D_{\text{ave}}^{\text{d}}$ (nm)	Pore Volume (cm^3g^{-1})		
	$S_{\text{micro}}^{\text{a}}$	$S_{\text{ext}}^{\text{b}}$	$S_{\text{BET}}^{\text{c}}$		$V_{\text{micro}}^{\text{e}}$	$V_{\text{meso+macro}}^{\text{f}}$	V_{t}^{g}
C-S0	331.634	82.160	413.794	2.247	0.173	0.059	0.232
AC-S1M	344.483	74.212	418.695	2.171	0.173	0.054	0.227
AC-S2M	340.287	109.129	449.416	2.132	0.171	0.069	0.240
AC-S4M	376.382	95.263	471.645	2.145	0.185	0.068	0.253

^a S_{micro} : micropore surface area.

^b S_{ext} : external surface area.

^c S_{BET} : Brunauer-Emmett-Teller surface area.

^d D_{ave} : average pore size ($4V_{\text{t}}/S_{\text{BET}}$).

^e V_{micro} : micropore volume.

^f $V_{\text{meso+macro}}$: mesopore and macropore volume.

^g V_{t} : total volume at P/P_0 of 0.997.

of the graphite layers. The G band is associated with the Irregularities in the arrangement of the graphite layer and levels of electrical conductivity. In the C-S0 sample, an $I_{\text{D}}/I_{\text{G}}$ ratio of 1.258 is in the D band (1348.667 cm^{-1}) and G band (1588.518 cm^{-1}). The AC-S4M sample shows an $I_{\text{D}}/I_{\text{G}}$ ratio of 1.243 in the D band (1358.519 cm^{-1}) and G band (1593.114 cm^{-1}) positions. The elevated $I_{\text{D}}/I_{\text{G}}$ ratio observed in the AC-S4M sample signifies increased structural irregularities in the carbon and a reduction in crystal size. The results presented here corroborate

those obtained from SEM analysis. The peaks of the D band and G band are vibrational modes of sp^2 -bonded carbon atoms, which indicate the presence of an irregular microcrystalline structure or amorphous structure. The increase in FWHM in band D in the AC-S4M sample shows that defective species in the sp^2 clusters increase due to the influence of chemical activation. Raman characterization shows results that are in accordance with XRD characterization.

Fig. 5 presents the FTIR characterization results of activated carbon

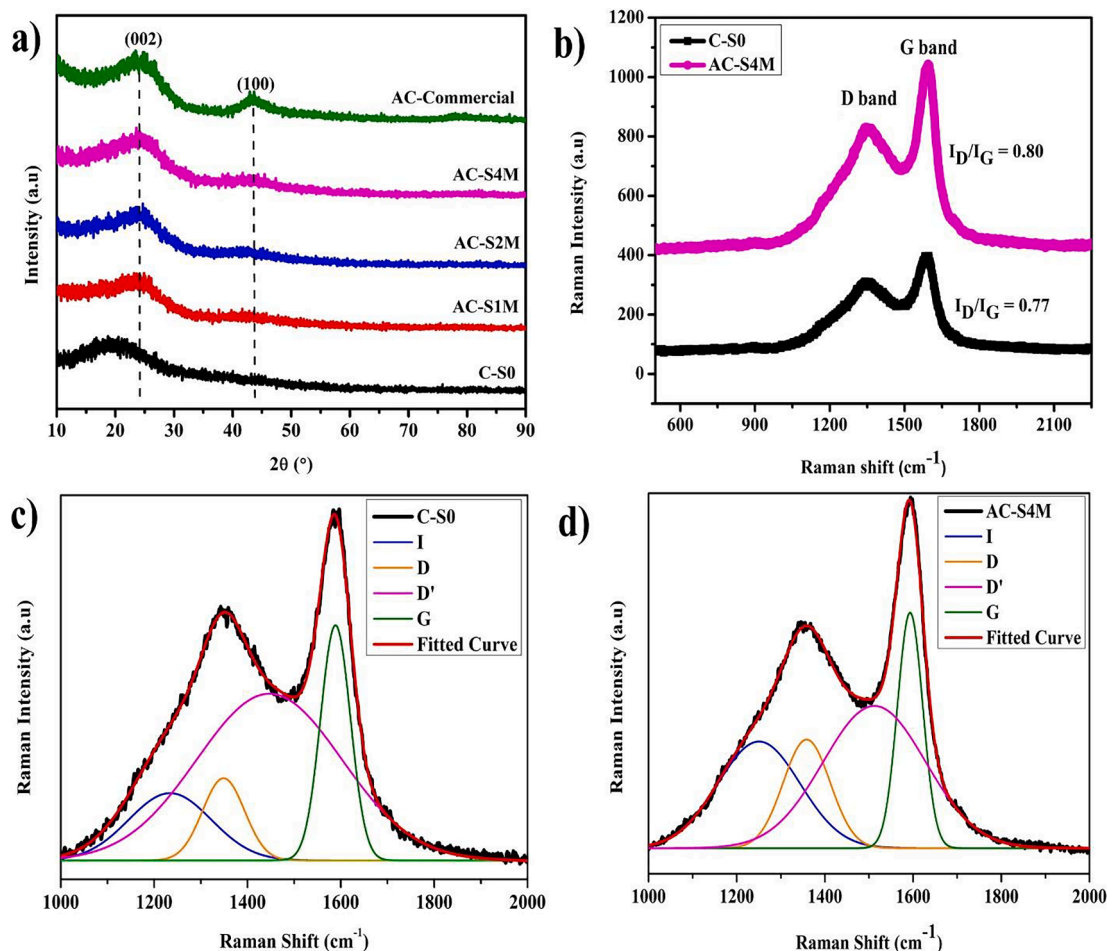


Fig. 4. (a) XRD diffraction pattern, (b) Raman spectra, (c) Raman deconvolution curve of the C-S0 sample, (d) Raman deconvolution curve of the AC-S4M sample.

Table 3

Raman parameter analysis of *Manihot esculenta*-tuber activated carbon.

Sample	Raman shift (cm^{-1}) of each parameter				FWHM _D ^e
	I ^a	D ^b	D' ^c	G ^d	
C-S0	1233.943	1348.667	1446.767	1588.518	105.905
AC-S4M	1250.392	1358.519	1512.185	1593.114	125.440

^a I: impurities in the structure of graphite.

^b D: defect carbon in the activated carbon structure.

^c D': Irregularities in the arrangement of graphene layer.

^d G: graphitic order.

^e FWHM_D: full width at the half maximum of D-band peak.

derived from *Manihot esculenta* tubers at different KOH concentrations. FTIR spectroscopy was employed to characterize the functional groups of activated carbon produced from *Manihot esculenta* tubers. Based on Fig. 5, the *Manihot esculenta* tubers activated carbon functional group has a wave number range of 526–3629 cm^{-1} with increasing and decreasing absorption peaks. The FTIR spectrum of the C-S0 sample is different from the FTIR spectrum of the AC-S1M, AC-S2M, and AC-S4M samples. The samples with chemical activation have a uniform shape. The activation process produces an O – H (hydroxyl) absorption peak for the phenolic functional group located at 3632.60 cm^{-1} for AC-S1M, AC-S2M, and 3643.19 cm^{-1} for AC-S4M. The activation process, involving KOH and subsequent carbonation, decomposes phenolic compounds, releasing carbon dioxide gas. The gas evolution contributes to enhanced porosity and surface area development in the activated carbon derived from *Manihot esculenta* tubers (Darvishi et al., 2021). The

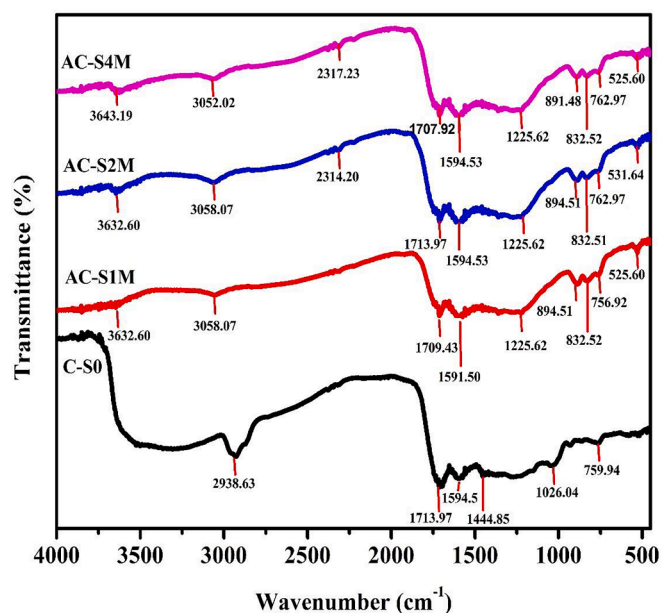


Fig. 5. FTIR spectra of *Manihot esculenta* tubers-activated carbon at various concentrations of KOH activator.

presence of hydroxyl groups (O – H), evidenced by the absorption band between 3200 and 3850 cm^{-1} , suggests residual water content from the activation process (Ospino Orozco et al., 2022). At wave numbers 2927–3056 cm^{-1} , the aliphatic C – H functional group has a low absorption peak in samples AC-S1M, AC-S2M, and AC-S4M. The decrease in the absorption peak can be explained by the loss of hydrogen (H) atoms, which evaporate during the activation phase (Mopoung et al., 2015). The wave number range 1600–1820 cm^{-1} contains the C = O functional group, located at a wavelength of 1716.41 cm^{-1} . The presence of lignin in the activated carbon derived from *Manihot esculenta* tubers is indicated by the C = O functional group. In the wave number range 1553–1635 cm^{-1} , there is a C = C functional group. The activated carbon derived from *Manihot esculenta* tubers showed a C = C group at 1586.56 cm^{-1} . The C = C group indicates the presence of aromatic compounds that make up the hexagonal structure of activated carbon. The presence of a C – O group at 1228.9 cm^{-1} indicates the polar nature and high absorption capacity of *Manihot esculenta* tubers-activated carbon (Wijaya et al., 2018). The C – C functional groups were between wave numbers 767.05 to 903.12 cm^{-1} , indicating the presence of cellulose in activated carbon. In activated carbon samples that have been activated using KOH, the aromatic C – H functional groups are detected at wavenumbers of 832 cm^{-1} and 525 cm^{-1} . The aromatic C – H group shows that there are pores on the surface of the activated carbon (Baloch et al., 2021; Wang et al., 2021b).

The XPS spectra results show further analysis of the chemical elements of *Manihot esculenta* tubers activated carbon at a 4 M

concentration of KOH activator, as presented in Fig. 6. Based on Fig. 6 (a), the XPS observed spectrum of *Manihot esculenta* tubers activated carbon at a 4 M concentration of KOH activator shows the presence of carbon, oxygen, and silicon elements. The high-resolution O1s XPS spectrum in Fig. 6(b) deconvoluted into three components, corresponding to C–O (533.90 eV), C–O–C (532.29 eV), and C = O (530.85 eV) bonds, respectively (Wang et al., 2021b). The C–O–C bond exhibits an area percentage of 56.44 %, surpassing the C = O bond at 24 % and C–O at 19.55 %. A high C–O–C bond percentage indicates the presence of an ether group, which influences the absorption capacity from activated carbon. Fig. 6(c) illustrates three distinct chemical states of carbon, each characterized by different peaks. Deconvolution of the C1s peak reveals three distinct components centered at 288.69 eV (C = C aromatic), 286.42 eV (C–O), and 284.79 eV (C–C), with the C–C component exhibiting the highest peak area (Owusu et al., 2020). In line with the FTIR characterization results, the C–C bonds are attributed to the cellulose content present in *Manihot esculenta* tubers. Meanwhile, as depicted in Fig. 6(d), the SiO₂ presence is evident in the Si 2p peak, displaying a low peak intensity at the binding energy position of 102.43 eV. The Si 2p peak is derived from the precursor content of *Manihot esculenta* tubers, which persists even after activation. The presence of Si 2p peak was observed in activated carbon derived from rice husk (Barakat et al., 2022).

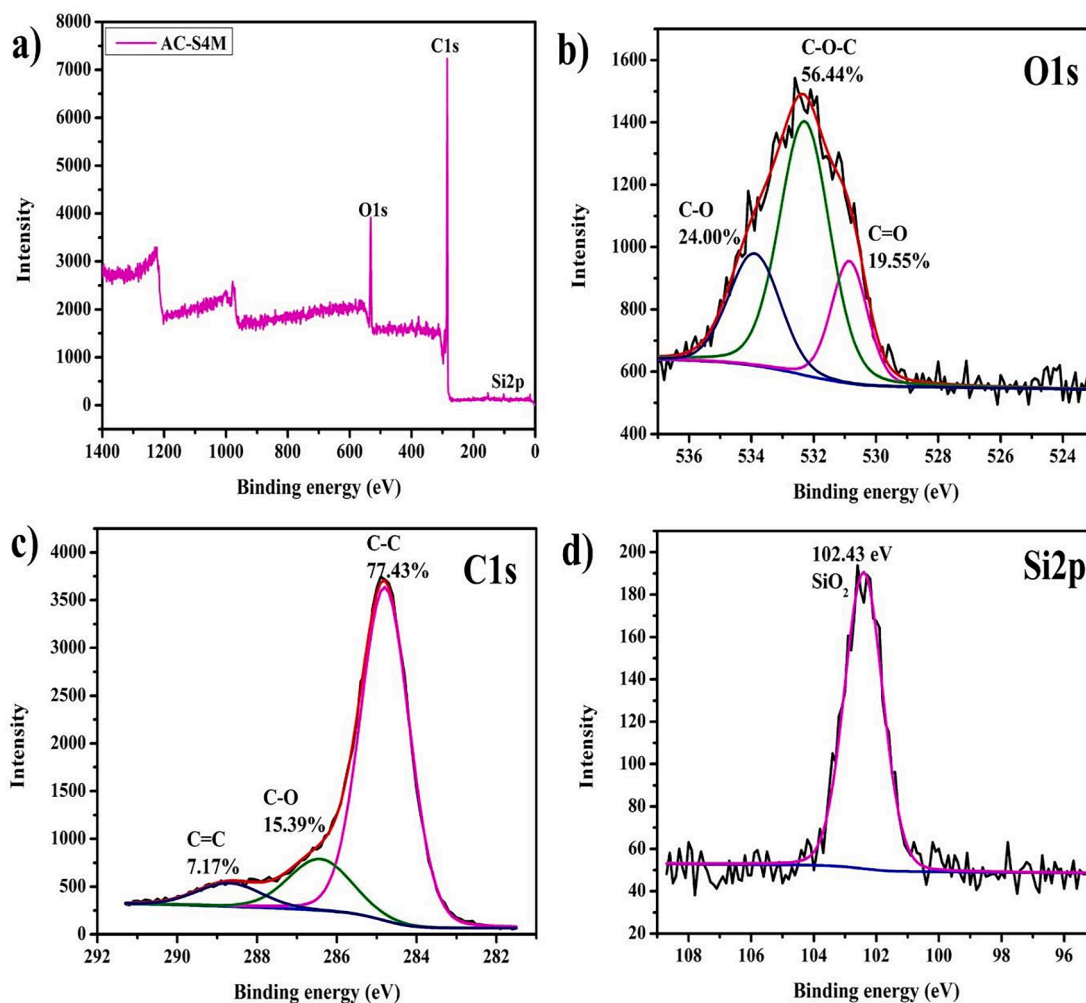


Fig. 6. XPS spectrum of *Manihot esculenta* tubers-activated carbon at 4 M KOH activator concentration, (a) survey spectrum, (b) O1s spectrum, (c) C1s spectrum, and (d) Si2p spectrum.

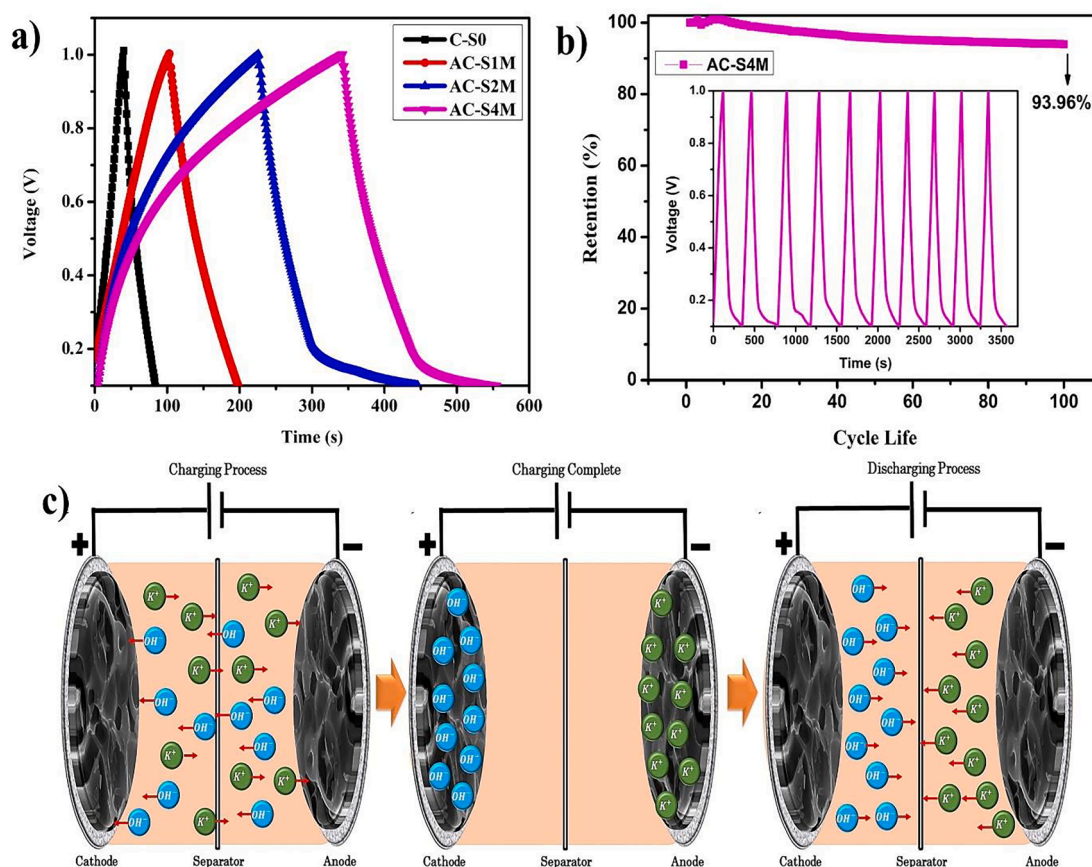


Fig. 7. (a) GCD curves, (b) capacitance retention, and (c) the coin cell supercapacitor configuration scheme during the charging and discharging process.

3.2. Electrochemical performance

Fig. 7(a) shows the charge–discharge graph that was performed at various KOH concentrations on supercapacitor electrodes made of carbon activated by *Manihot esculenta* tubers. The GCD in Fig. 7(a) shows the ability to charge and discharge the supercapacitor electrodes from 0 V to 1 V. Fig. 7(b) illustrates the stability retention of the AC-S4M sample, demonstrating a retention rate of 93.96 % at the 100th cycle. The initial increase in retention over the first 20 cycles suggests the activation of the electrode during the charge–discharge process (Selvaraj et al., 2020). The charging process occurs when the supercapacitor undergoes a transient phase following the application of a supply voltage. The higher voltage with increasing time indicates that the *Manihot esculenta* tubers-activated carbon electrode responds fast to an electric field. The higher voltage during the charging process also demonstrates the capability of the electric field to orient activated carbon molecules, leading to polarization within the supercapacitor (Vinayagam et al., 2021). During discharge, a significant electric charge is transferred to the resistance. The transfer is evident from the voltage, which decreases sharply when the discharge process begins (Diantoro et al., 2022). Fig. 7(c) depicts the configuration of the coin cell supercapacitor during charging and discharging processes. The resulting graph forms an imperfectly symmetrical triangle, which characterizes the EDLC supercapacitor (Wei et al., 2020).

GCD graphs can be processed to produce specific capacitance, energy density, and power density, as shown in Table 4, which illustrates the impact of increased KOH concentration on these parameters. The AC-S4M sample demonstrates the highest performance, signifying that the electrode can store significant electrolyte ions. Optimizing the ion-transfer pathway is essential for improving electrolyte accessibility to the micropore structure (Vinayagam et al., 2020). The performance is

Table 4

The specific capacitance, energy density, and power density the *Manihot esculenta* tubers activated carbon electrode-based coin cell supercapacitor.

Sample	Specific Capacitance (Fg^{-1})	Energy Density (Whkg^{-1})	Power Density (Wkg^{-1})
C-S0	20.03	2.051	171.740
AC-S1M	43.36	4.529	173.44
AC-S2M	97.51	10.242	173.920
AC-S4M	146.57	15.525	174.660

corroborated by BET analysis, which reveals the presence of microporous structures in the activated carbon, leading to high-performance supercapacitors (Vinayagam et al., 2024a). Nickel foam substrates enhance the active surface area and improve the interface for electrolyte ion diffusion, effectively capturing electrons and providing a robust pathway for electrolyte ion transport. The comparison of electrochemical supercapacitors derived from biomass-activated carbon using KOH activators is presented in Table 5.

Fig. 8(a) and Fig. 7(b) display the CV curves of the EDLC supercapacitor coin cell, which reveal a quasi-rectangular shape representing the relationship between voltage and current. Based on the graph, there are two types of currents. The charge current (I_c) is shown in the voltage range of -0.4 to 1.0 V, and the output current (I_d) is in the voltage range of 1.0 to -0.4 V. Fig. 8(a) at a scan rate of 80 mVs^{-1} is rectangular with a more prominent curve area when the KOH concentration is increased. The AC-S4M sample exhibited the largest cyclic voltammetry curve area, suggesting rapid electrolyte ion diffusion, and has the highest specific capacitance. Fig. 8(b) shows the CV on the AC-S4M sample at different

Table 5
Performance comparison of supercapacitor from activated carbon biomass with KOH activator.

Biomass	Activating Agent	Specific Capacitance (Fg ⁻¹)	Energy Density (Whkg ⁻¹)	Power Density (Wkg ⁻¹)	R _{ct} (Ω)	Electrochemical Measurements	Ref.
Cocoa Skin	KOH 0.4 M	140.2	–	–	–	Three electrode system	(Yuli et al., 2021)
Sugarcane Bagasse	KOH 0.3 M	146.89	3.83	209	1.59	Supercapacitor cell	(Taer et al., 2014)
Banana stem	KOH 0.5 M	170	–	–	3.80	Sandwich type	(K et al., 2017)
Coffee	KOH 1:1 ratio	74	–	–	–	Coin cell device	(Choi et al., 2019)
Manihot esculenta peel	KOH 70 %	62.16	–	–	–	Three electrode system	(Ospino Orozco et al., 2022)
Pomelo peel	KOH 1:4 ratio	43.5	17.1	420	0.47	Three electrode system	(Peng et al., 2014)
Cigarette filters	KOH	52	7.2	127	–	Sandwich type	(Bi et al., 2022)
Sweet corn husks	KOH 1:4 ratio	80	20	0.68	7.80	Coin cell device	(Usha Rani et al., 2020)
Rice Straw	KOH 1:3 ratio	80	17.4	126	–	Three electrode system	(Sudhan et al., 2017)
Baobab fruit shells	KOH 1:1 ratio	56.67	20.86	400	2.06	Solid-state supercapacitor device	(Mohammed et al., 2019)
Cocos nurifera	ZnCl ₂ and KOH	279.56	7.52	220.00	–	two-symmetric electrode system	(Subraya Hegde and Ramachandra Bhat, 2024)
Mangifera indica leaf	FeCl ₃ , KOH	521.65	17.04	242.50	–	two symmetric electrode system	(Hegde and Bhat, 2024a)
Tectona grandis	FeCl ₃ , KOH	572.0	–	–	–	two symmetric electrode system	(Hegde and Bhat, 2024b)
Fatsia Japonica seed	KOH	140	23	550	1.50	Coin cell device	(Li et al., 2020)
Manihot esculenta tuber	KOH 4 M	147.57	15.53	174.66	2.19	Coin cell device	This work

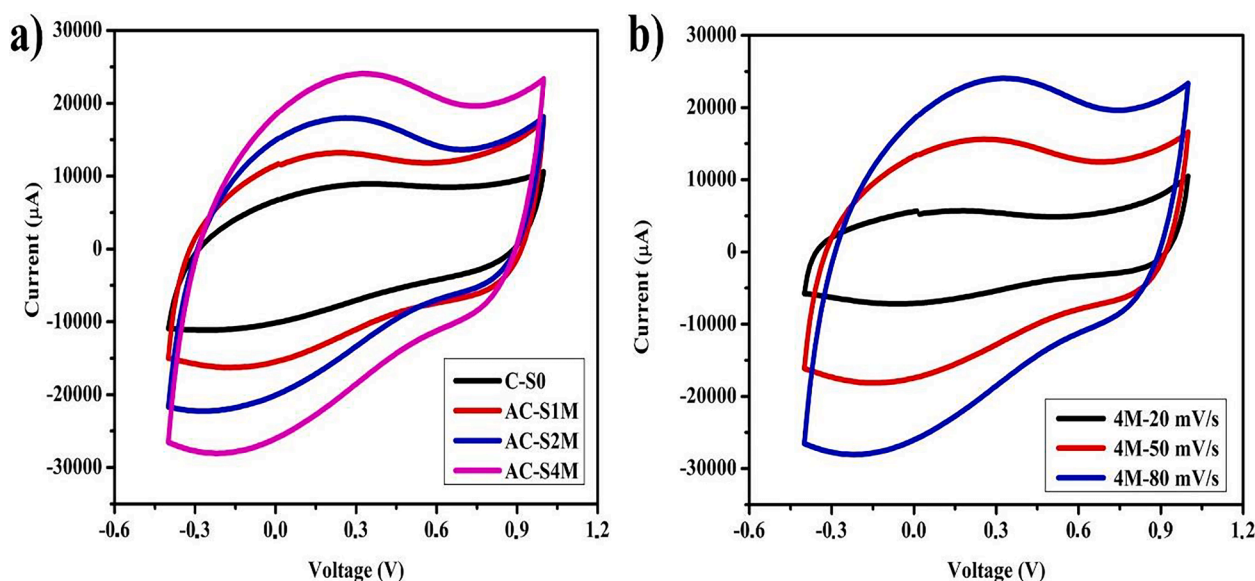


Fig. 8. (a) CV curves with scan rate 80 mV/s, (b) CV curves AC-S4M sample.

scan rates of 20, 50, and 80 mVs⁻¹. The graph shows the characteristics of an EDLC supercapacitor with a rectangular curve. Increased scan rate during cyclic voltammetry measurements resulted in a larger enclosed area, indicating a higher electrochemical performance associated with lower internal resistance at the electrode–electrolyte interface (Thirumal et al., 2022). Activated carbon in a sponge can retain electrolyte ions, thereby increasing charge storage capacity and improving supercapacitor performance (Lobato-Peralta et al., 2023). Fig. 9(a and b) illustrate the Ragone plot and correlation between the pore structure of activated carbon and the specific capacitance of the supercapacitor (Chaitra et al., 2017; Qian et al., 2014; Wang et al., 2021a; Wang et al., 2013, 2020; Young et al., 2022). Based on Fig. 9(a), activated carbon derived from Manihot esculenta exhibits superior power density compared to activated carbon sourced from *Nipah fruticans* fruit, bamboo stalk, *Shorea robusta* wood dust, and bamboo carbon (Farma et al., 2021a; Gong et al., 2017; Muthi Aturoifah et al., 2024; Shrestha

and Rajbhandari, 2021).

Further investigation in term of electrochemical performance of supercapacitors based on Manihot esculenta tubers-derived activated carbon was conducted through EIS, which provided insights into impedance and resistance capabilities. Impedance is related to capacitive performance or alternating current movement, while resistance is related to resistance from a device or direct current movement (Gharbi et al., 2020; Kim et al., 2019). The data obtained from the EIS is in the form of a Nyquist plot. The Nyquist plot is shown from the real (Z') and imagined (Z'') impedance values, as shown in Fig. 10(a). Fig. 10(a) shows a smaller diameter of quasi-semicircle with increasing KOH concentration. The diameter of the quasi-semicircle represents the charge transfer resistance of cations from the electrolyte to the electrode matrix (R_{ct}). Electrochemical performance is better if the device resistance is low, indicated by a small R_{ct} (Hasan et al., 2022; Shahrokhian et al., 2018; Thirumal et al., 2022). The R_{ct} is an essential indicator for

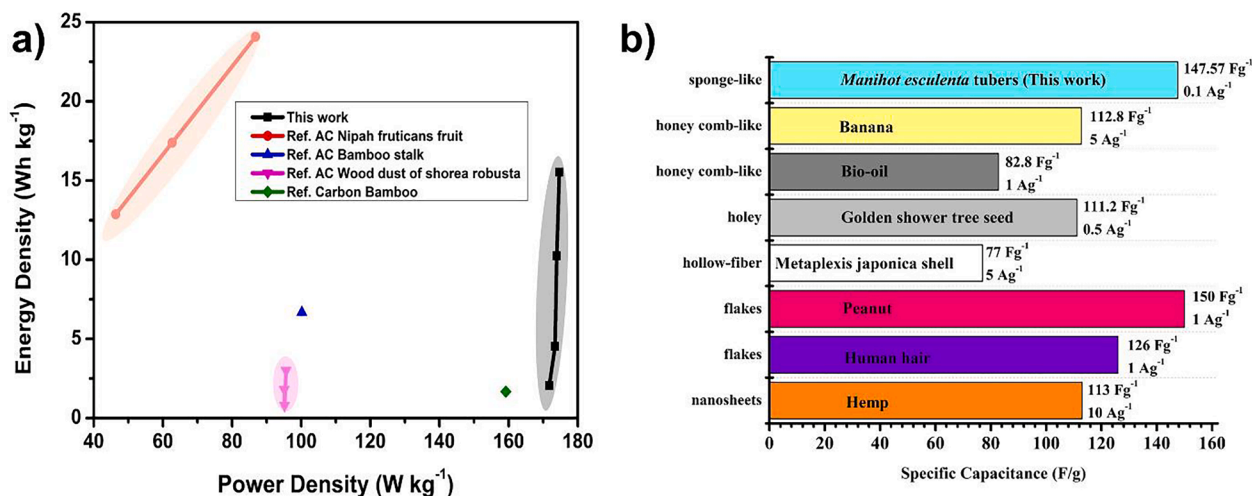


Fig. 9. (a) Ragone plot of the *Manihot esculenta* activated carbon supercapacitor compared with different biomass, (b) the comparison of the pore shape of activated carbon with the specific capacitances.

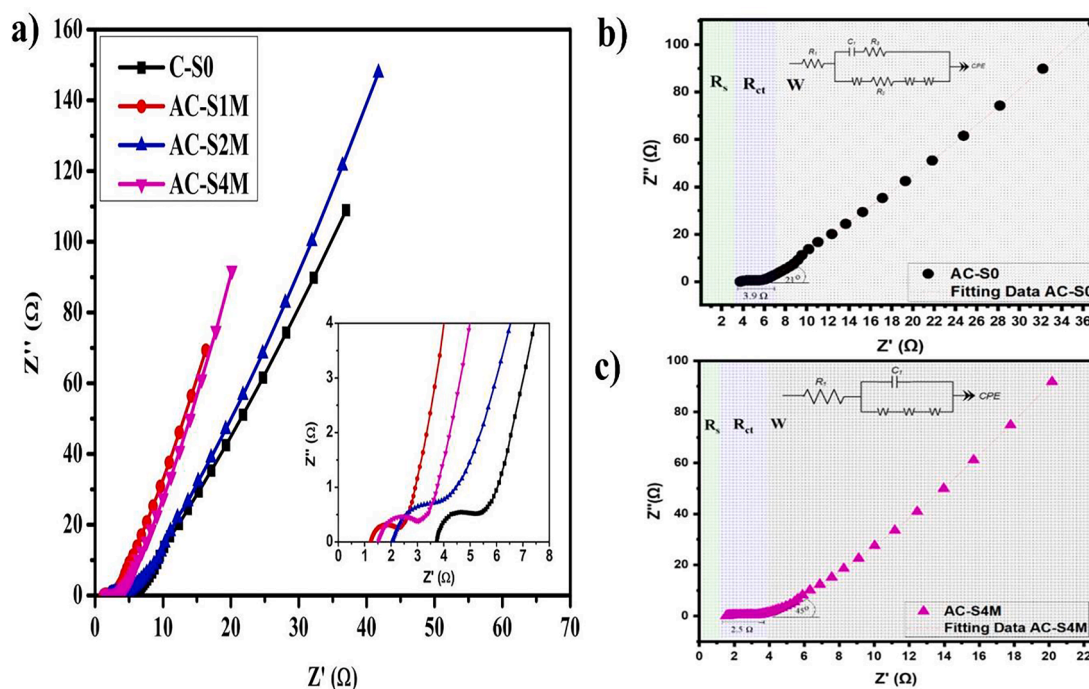


Fig. 10. (a) Nyquist plot of *Manihot esculenta* tubers-activated carbon electrodes, fitting of the EIS data using an equivalent circuit model for supercapacitor coin cell (b) C-S0 and (c) AC-S4M.

determining the electrochemical rate of supercapacitors (Muthurasu and Ganesh, 2012). The increase in the electrochemical performance is associated with the decrease in initial resistance (R_s) and R_{ct} (Charoensook et al., 2021b).

Fig. 10(b and c) shows that comparing the Nyquist fitting data for sample C-S0 and sample AC-S4M, sample C-S0 has higher resistance

Table 6
Equivalent circuit Randles model for C-S0 and AC-S4M.

Sample	R_s (Ω)	R_{ct} (Ω)	C (F)	W_o (Ω)	W_s (Ω)	W (Ω)
C-S0	3.1	4.3069	1.66×10^{-5}	5.2292	1.65×10^{-6}	4.19×10^{-7}
AC-S4M	0.7	2.1903	1.205×10^{-4}	2.3577	0.25801	0.92299

than sample AC-S4M. Sample AC-S4M has lower R_s and R_{ct} than sample C-S0. Based on Table 6, the R_{ct} is 4.3 Ω for the C-S0 sample and 2.2 Ω for the AC-S4M sample. Apart from R_{ct} , R_s is also an important indicator of supercapacitor performance. R_s represents the overall resistance, encompassing both the bulk resistance of the electrolyte and the interfacial resistance at the electrode–electrolyte interface. The R_s on C-S0 and AC-4 M are 3.1 and 0.7 Ω. Less resistance in the electrolyte pathway is characterized by lower R_s and R_{ct} , thereby increasing conductivity and device performance. Fig. 10(b and c) shows illustrates a Randles equivalent circuit model consisting of internal resistance (R_s) in series with a capacitance (C_1) connected in parallel by a combination of charge transfer resistance (R_{ct}) and Warburg impedance (ZW) with a Warburg element (W open, W short, and W) as shown in Table 6.

Table 6 shows that decreased R_s and R_{ct} increase the C, indicating the capacitance performance. Based on the EIS analysis results, an increased

slope in the impedance plot correlates with improved electrochemical performance and higher capacitance values (Funari et al., 2020; Song et al., 2018; Zelinsky et al., 2022). In addition to the semi-circular graph representing R_s and R_{ct} , the straight line shows the Warburg area. The straight-line Warburg impedance (W) indicates the ion diffusion path capability, which is influenced by the capacitive properties of the material (Kurniawan et al., 2019; Zeigler et al., 2015). Several factors influence Warburg impedance, including electrolyte, morphology, and electrode material composition (Koseoglou et al., 2021; Laschuk et al., 2021). The optimal supercapacitor performance is achieved at a 45° angle on the Warburg line, owing to the equilibrium between diffusion and electrochemical reactions. The slope of the Warburg line shows that there is less resistance when electrons move between the electrode and the electrolyte (Lukács and Kristóf, 2020). Fig. 10(c) shows that the AC-S4M sample performs better, with the Nyquist forming an angle of 45° compared to the C-S0 sample. An angle slope approaching 90° signifies enhanced capacitive behavior within a device, characterized by the facile movement of KOH within the pores and rapid ionic diffusion (Chaudhary et al., 2019; Moreno-Fernández et al., 2019). The mechanism aligns with a report using NAC electrodes, which exhibited a significantly lower Warburg impedance (0.5291 Ω) compared to AC electrodes (0.8383 Ω), indicating better electronic conductivity (Abouelamaiem et al., 2018; Iqbal et al., 2020). The findings confirm that AC-S4M sample exhibits superior electrochemical and ionic diffusion performance compared to samples with lower KOH concentrations.

4. Conclusion

Manihot esculenta tubers-derived activated carbon demonstrates strong potential as a sustainable and efficient electrode material for supercapacitors, addressing the limitations of conventional capacitors. By employing chemical activation with varying KOH concentrations (0, 1, 2, and 4 M), we achieved a distinctive, sponge-like porous morphology, which is particularly pronounced in the optimized AC-S4M sample. This sample exhibited the highest surface area (471.65 m²g⁻¹) and ideal pore diameter (2.67 nm), enhancing ion transport and electrolyte accessibility. *Manihot esculenta* tubers activated carbon has an amorphous structure with diffraction peaks at (002) and (100). Through a chemical activation process, activated carbon is produced, which is indicated by the functional groups C = O, C = C, C – O, and C – H. The symmetric supercapacitor coin cell utilizing AC-S4M achieved an impressive gravimetric capacitance of 146.57 Fg⁻¹ at 0.1 Ag⁻¹, and in a 6 M KOH aqueous electrolyte, delivered a high energy density of 15.525 Whkg⁻¹ at a power density of 174.660 Wkg⁻¹ with an R_{ct} of 2.19 Ω . These findings establish *Manihot esculenta* tubers-derived carbon as a viable option for high-performance, scalable supercapacitor electrodes, advancing the development of sustainable energy storage solutions.

CRedit authorship contribution statement

Markus Diantoro: Writing – review & editing, Supervision, Conceptualization. **Nuviya Illa Muthi Aturroifah:** Writing – original draft, Methodology, Formal analysis. **Joko Utomo:** Writing – review & editing, Data curation. **Ishmah Luthfiyah:** Visualization, Formal analysis. **Ida Hamidah:** Writing – review & editing. **Brian Yulianto:** Writing – review & editing. **Andriwo Rusydi:** Writing – review & editing. **Worawat Meevesana:** . **Santi Maensiri:** . **Pramod K. Singh:** Writing – review & editing.

Declaration of Competing Interest

The authors declare that they have no known competing financial interests or personal relationships that could have appeared to influence the work reported in this paper.

Acknowledgments

The authors would like to acknowledge the Ministry of Culture, Higher Education, Research, Technology of the Republic of Indonesia and Universitas Negeri Malang through Riset Kolaborasi Indonesia 2022 research grant.

Funding

This research was funded by the national competitive grant of Riset Kolaborasi Indonesia 2022 from the Ministry of Higher Education, Research and Technology with a specific grant by Universitas Negeri Malang, Contract No. 17.5.51/UN32.20.1/LT/2022.

References

- Abouelamaiem, D.I., He, G., Parkin, I., Neville, T.P., Jorge, A.B., Ji, S., Wang, R., Titirici, M.M., Shearing, P.R., Brett, D.J.L., 2018. Synergistic relationship between the three-dimensional nanostructure and electrochemical performance in biocarbon supercapacitor electrode materials. *Sustain. Energy Fuels* 2, 772–785. <https://doi.org/10.1039/c7se00519a>.
- Adinaveen, T., Kennedy, L.J., Vijaya, J.J., Sekaran, G., 2013. Studies on structural, morphological, electrical and electrochemical properties of activated carbon prepared from sugarcane bagasse. *J. Ind. Eng. Chem.* 19, 1470–1476. <https://doi.org/10.1016/j.jiec.2013.01.010>.
- Adoor, P., Hegde, S.S., Bhat, B.R., Yethadka, S.N., Yeenduguli, R., 2023. Elucidating the role of copper-induced mixed phases on the electrochemical performance of Mn-based thin-film electrodes. *ACS Omega* 8, 46640–46652. <https://doi.org/10.1021/acsomega.3c05614>.
- Adoor, P., Hegde, S.S., Bhat, B.R., George, S.D., Yeenduguli, R., 2024. Electrochemical performance and structural evolution of spray pyrolyzed Mn3O4 thin films in different aqueous electrolytes: effect of anions and cations. *RSC Adv.* 14, 29748–29762. <https://doi.org/10.1039/D4RA05426A>.
- Agadi, N.P., Hegde, S.S., Teradal, N.L., Bhat, B.R., Seetharamappa, J., 2024. Unveiling the versatile applications of cobalt oxide-embedded nitrogen-doped porous graphene for enhanced energy storage and simultaneous determination of ascorbic acid, dopamine and uric acid, 097510 *J. Electrochem. Soc.* 171. <https://doi.org/10.1149/1945-7111/ad798d>.
- Ahmed, S., Rafat, M., Ahmed, A., 2018. Nitrogen doped activated carbon derived from orange peel for supercapacitor application, 035008 *Adv. Nat. Sci. Nanosci. Nanotechnol.* 9. <https://doi.org/10.1088/2043-6254/aad5d4>.
- Atchudan, R., Jebakumar Immanuel Edison, T.N., Perumal, S., Vinodh, R., Babu, R.S., Sundramoorthy, A.K., Renita, A.A., Lee, R., 2022. Facile synthesis of nitrogen-doped porous carbon materials using waste biomass for energy storage applications. *Chemosphere* 289, 133225. <https://doi.org/10.1016/j.chemosphere.2021.133225>.
- Baig, M.M., Gul, I.H., 2021. Conversion of wheat husk to high surface area activated carbon for energy storage in high-performance supercapacitors. *Biomass Bioenergy* 144, 105909. <https://doi.org/10.1016/j.biombioe.2020.105909>.
- Baloch, H.A., Nizamuddin, S., Siddiqui, M.T.H., Riaz, S., Konstas, K., Mubarak, N.M., Srinivasan, M.P., Griffin, G.J., 2021. Catalytic upgradation of bio-oil over metal supported activated carbon catalysts in sub-supercritical ethanol. *J. Environ. Chem. Eng.* 9, 105059. <https://doi.org/10.1016/j.jece.2021.105059>.
- Barakat, N.A.M., Irfan, O.M., Moustafa, H.M., 2022. H3PO4/KOH Activation Agent for High Performance Rice Husk Activated Carbon Electrode in Acidic Media Supercapacitors. *Molecules* 28, 296. <https://doi.org/10.3390/molecules2810296>.
- Bi, R., Pang, S.-K., Yung, K.-C., Yin, L.-K., 2022. Comprehensive study of used cigarette filters-derived porous activated carbon for Supercapacitors: From biomass waste to sustainable energy source. *J. Electroanal. Chem.* 925, 116915. <https://doi.org/10.1016/j.jelechem.2022.116915>.
- Borenstein, A., Hanna, O., Attias, R., Luski, S., Brousse, T., Aurbach, D., 2017. Carbon-based composite materials for supercapacitor electrodes: a review. *J. Mater. Chem. A* 5, 12653–12672. <https://doi.org/10.1039/C7TA00863E>.
- Chaisit, S., Chanlek, N., Khajonrit, J., Sichumsaeng, T., Maensiri, S., 2020. Preparation, characterization, and electrochemical properties of KOH-activated carbon from cassava root. *Mater. Res. Express* 7, 105605. <https://doi.org/10.1088/2053-1591/abbf84>.
- Chaitra, K., Vinny, R.T., Sivaraman, P., Reddy, N., Hu, C., Venkatesh, K., Vivek, C.S., Nagaraju, N., Kathyayini, N., 2017. KOH activated carbon derived from biomass-banana fibers as an efficient negative electrode in high performance asymmetric supercapacitor. *J. Energy Chem.* 26, 56–62. <https://doi.org/10.1016/j.jechem.2016.07.003>.
- K. Charoensook, C. Huang, H. Tai, Y. Li. 2021b. Journal of the Taiwan Institute of Chemical Engineers Preparation of porous nitrogen-doped activated carbon derived from rice straw for high-performance supercapacitor application. 120. 246–256. <https://doi.org/10.1016/j.jtice.2021.02.021>.
- Charoensook, K., Huang, C.-L., Tai, H.-C., Lanjapalli, V.V.K., Chiang, L.-M., Hosseini, S., Lin, Y.-T., Li, Y.-Y., 2021a. Preparation of porous nitrogen-doped activated carbon derived from rice straw for high-performance supercapacitor application. *J. Taiwan Inst. Chem. Eng.* 120, 246–256. <https://doi.org/10.1016/j.jtice.2021.02.021>.

- Chaudhary, P., Bansal, S., Sharma, B.B., Saini, S., Joshi, A., 2024. Waste biomass-derived activated carbons for various energy storage device applications: A review. *J. Energy Storage* 78, 109996. <https://doi.org/10.1016/j.est.2023.109996>.
- Chaudhary, S., Kuntal, D., Althurthi Bharani Venkata, K.K., Veera Venkata, R.C., Goli, N., Thomas, S., 2019. Nanocomposite having Flower -Shaped Morphology as Electrode for Electrochemical Supercapacitor Applications. *ChemistrySelect* 4, 8719–8726. <https://doi.org/10.1002/slct.201900899>.
- Chen, Y., Zhang, X., Zhang, H., Sun, X., Zhang, D., Ma, Y., 2012. High-performance supercapacitors based on a graphene-activated carbon composite prepared by chemical activation. *RSC Adv.* 2, 7747. <https://doi.org/10.1039/c2ra20667f>.
- Chen, W., Zhou, X., Shi, S., Thiphuong, N., Chen, M., 2017. Synergistical enhancement of the electrochemical properties of lignin-based activated carbon using NH₃-H₂O dielectric barrier discharge plasma. *RSC Adv.* 7, 7392–7400. <https://doi.org/10.1039/C6RA26010A>.
- Choi, J., Zequine, C., Bhojate, S., Lin, W., Li, X., Kahol, P., Gupta, R., 2019. Waste coffee management: deriving high-performance supercapacitors using nitrogen-doped coffee-derived carbon. *J. Carbon Res.* 5, 44. <https://doi.org/10.3390/c5030044>.
- Darvishi, C., Zohreh, A.-K., Neda, S., Seyedmehdi, S., Mika, 2021. Ce and Mn/bio-waste-based activated carbon composite: Characterization, phenol adsorption and regeneration, 105788 *J. Environ. Chem. Eng.* 9. <https://doi.org/10.1016/j.jece.2021.105788>.
- De Boer, J., 1965. Studies on pore systems in catalysts VII. Description of the pore dimensions of carbon blacks by the t method. *J. Catal.* 4, 649–653. [https://doi.org/10.1016/0021-9517\(65\)90264-2](https://doi.org/10.1016/0021-9517(65)90264-2).
- Demir, M., Doguscu, M., 2022. Preparation of Porous Carbons Using NaOH, K₂CO₃, Na₂CO₃ and Na₂S₂O₃ Activating Agents and Their Supercapacitor Application: A Comparative Study. *ChemistrySelect* 7. <https://doi.org/10.1002/slct.202104295>.
- Diantoro, M., Luthfiyah, I., Wisodo, H., Utomo, J., Meevasana, W., 2022. Electrochemical performance of symmetric supercapacitor based on activated carbon biomass TiO₂ nanocomposites. *J. Phys. Conf. Ser.* 2243, 12–77.
- Farma, R., Lestari, A.N.I., Apriyani, I., 2021a. Supercapacitor cell electrodes derived from nipah fruticans fruit coir biomass for energy storage applications using acidic and basic electrolytes. *J. Phys. Conf. Ser.* 2049, 012043. <https://doi.org/10.1088/1742-6596/2049/1/012043>.
- Farma, R., Lestari, O., Taer, E., Apriwandi, M., Awitdrus, A., 2021b. Removal of Cu, Fe, and Zn from peat water by using activated carbon derived from oil palm leaves. *Adv. Mater. Res.* 1162, 65–73. <https://doi.org/10.4028/www.scientific.net/AMR.1162.65>.
- Funari, R., Matsumoto, A., De Bruyn, J.R., Shen, A.Q., 2020. Rheology of the Electric Double Layer in Electrolyte Solutions. *Anal. Chem.* 92, 8244–8253. <https://doi.org/10.1021/acs.analchem.0c00475>.
- Gharbi, O., Tran, M.T.T., Tribollet, B., Turmine, M., Vivier, V., 2020. Revisiting cyclic voltammetry and electrochemical impedance spectroscopy analysis for capacitance measurements. *Electrochim. Acta* 343. <https://doi.org/10.1016/J.ELECTACTA.2020.136109>.
- Ghosh, S., Santhosh, R., Jeniffer, S., Raghavan, V., Jacob, G., Nanaji, K., Kollu, P., Jeong, S.K., Grace, A.N., 2019. Natural biomass derived hard carbon and activated carbons as electrochemical supercapacitor electrodes. *Sci. Rep.* 9, 16315. <https://doi.org/10.1038/s41598-019-52006-x>.
- Gong, Y., Li, D., Luo, C., Fu, Q., Pan, C., 2017. Highly porous graphitic biomass carbon as advanced electrode materials for supercapacitors. *Green Chem.* 19, 4132–4140. <https://doi.org/10.1039/C7GC01681F>.
- Hasan, K., Bashir, S., Subramanian, R., Kasi, R., Kamran, K., Iqbal, J., Algarni, H., Al-Sehemi, A.G., Wageh, S., Pershaanaa, M., Kamarulazam, F., 2022. Poly (Vinyl Alcohol)/Agar Hydrogel Electrolytes Based Flexible All-in-One Supercapacitors with Conducting Polyaniline/Polypyrrole Electrodes. *Polymers (basel)*. 14, 4784. <https://doi.org/10.3390/polym14214784>.
- He, X., Ling, P., Yu, M., Wang, X., Zhang, X., Zheng, M., 2013. Rice husk-derived porous carbons with high capacitance by ZnCl₂ activation for supercapacitors. *Electrochim. Acta* 105, 635–641. <https://doi.org/10.1016/j.electacta.2013.05.050>.
- Hegde, S.S., Bhat, B.R., 2024a. Sustainable energy storage: Mangifera indica leaf waste-derived activated carbon for long-life, high-performance supercapacitors. *RSC Adv.* 14, 8028–8038. <https://doi.org/10.1039/D3RA08910J>.
- Hegde, S.S., Bhat, B.R., 2024b. Biomass waste-derived porous graphitic carbon for high-performance supercapacitors. *J. Energy Storage* 76, 109818. <https://doi.org/10.1016/j.est.2023.109818>.
- Illingworth, J.M., Rand, B., Williams, P.T., 2022. Understanding the mechanism of two-step, pyrolysis-alkali chemical activation of fibrous biomass for the production of activated carbon fibre matting. *Fuel Process. Technol.* 235, 107348. <https://doi.org/10.1016/j.fuproc.2022.107348>.
- Intan Subadra, S.U., Sutiami, R., Taufiq, A., Diantoro, M., Sunaryono, Arif, Hidayat, Mufti, N., Hidayat, N., Susanto, H., Ari Adi, W., 2019. Preparation and Characterization of Magnetite Nanoparticles Combined with Polyaniline and Activated Carbon. *IOP Conf. Ser. Earth Environ. Sci.* 276, 012041. <https://doi.org/10.1088/1755-1315/276/1/012041>.
- Iqbal, M.Z., Faisal, M.M., Meshal Alzaid, S.R.A., 2020. A facile approach to investigate the charge storage mechanism of MOF/PANI based supercapattery devices. *Solid State Ion.* 354, 115411. <https://doi.org/10.1016/j.ssi.2020.115411>.
- Kalu-Uka, G.M., Kumar, S., Kalu-Uka, A.C., Vikram, S., Ihekwe, G.O., Ranjan, N., Anosike-Francis, E.N., Prajapati, G., Nduba, A., Onwuvalu, A.P., Kumar, S., 2022. Production of Activated Carbon Electrode for Energy Storage Application in Supercapacitors via KOH Activation of Waste Termite Biomass. *Waste Biomass Valoriz.* 13, 2689–2704. <https://doi.org/10.1007/s12649-022-01680-6>.
- Kim, B.C., Manikandan, R., Yu, K.H., Park, M.S., Kim, D.W., Park, S.Y., Justin Raj, C., 2019. Efficient supercapattery behavior of mesoporous hydrous and anhydrous cobalt molybdate nanostructures. *J. Alloys Compd.* 789, 256–265. <https://doi.org/10.1016/j.jallcom.2019.03.033>.
- Koseoglou, M., Tsioumas, E., Papagiannis, D., Jabbour, N., Mademlis, C., 2021. A Novel On-Board Electrochemical Impedance Spectroscopy System for Real-Time Battery Impedance Estimation. *IEEE Trans. Power Electron.* 36, 10776–10787. <https://doi.org/10.1109/TPEL.2021.3063506>.
- Kurniawan, R.Y., Kurniawan, I.D.O., Atmaja, L., Widiastuti, N., 2019. Synthesis N-Doped Activated Carbon from Sugarcane Bagasse for CO₂ Adsorption. *IPTEK J. Technol. Sci.* 30, 80. <https://doi.org/10.12962/j20882033.v30i3.5469>.
- Laschuk, nadia o, Easton, e bradley, Zenkina, olena v, 2021. Reducing the resistance for the use of electrochemical impedance spectroscopy analysis in materials chemistry. *R. Soc. Chem.* 11, 27925–27936.
- Lasrado, D., Ahankari, S., Kar, K.K., 2021. Global Trends in Supercapacitors 329–365. https://doi.org/10.1007/978-3-030-68364-1_10.
- Latupeirissa, J., Tanasale, M.F.J.D.P., Dade, K., 2016. Carbon characterization from Candelnut Shells (Aleurites Moluccana (L) Willd) with XRD. *Indones. J. Chem. Res.* 3, 324–328.
- Li, H., Cao, L., Wang, F., Duan, G., Xu, W., Mei, C., Zhang, G., Liu, K., Yang, M., Jiang, S., 2020. Fatsia Japonica-Derived Hierarchical Porous Carbon for Supercapacitors With High Energy Density and Long Cycle Life. *Front. Chem.* 8. <https://doi.org/10.3389/fchem.2020.00089>.
- Lisneri, L., Rahmi, H.Y., Gomiyati, N.A., Darni, Y., Febriningrum, P.N., Azhar, A., 2021. Preparation and Characterization of Nanocrystalline Cellulose from Cassava Stem Wastes by Electromagnetic Induction. *J. Rekayasa Kim. Lingkungan.* 16, 109–117. <https://doi.org/10.23955/rkl.v16i2.21927>.
- Lobato-Peralta, D.R., Duque-Brito, E., Oruga, H.O., Arias, D.M., Cuentas-Gallegos, A.K., Okolie, J.A., Okoye, P.U., 2023. Sponge-like nanoporous activated carbon from corn husk as a sustainable and highly stable supercapacitor electrode for energy storage. *Diam. Relat. Mater.* 138, 110176. <https://doi.org/10.1016/j.diamond.2023.110176>.
- Lukács, Z., Kristóf, T., 2020. A generalized model of the equivalent circuits in the electrochemical impedance spectroscopy. *Electrochim. Acta* 363. <https://doi.org/10.1016/j.electacta.2020.137199>.
- Mohammed, A.A., Chen, C., Zhu, Z., 2019. Low-cost, high-performance supercapacitor based on activated carbon electrode materials derived from baobab fruit shells. *J. Colloid Interface Sci.* 538, 308–319. <https://doi.org/10.1016/j.jcis.2018.11.103>.
- Mopoung, S., Moonstri, P., Palas, W., Khumpai, S., 2015. Characterization and properties of activated carbon prepared from tamarind seeds by KOH activation for Fe (III) adsorption from aqueous solution. *J. World J.*
- Moreno-Fernández, G., Gómez-Urbano, J.L., Enterría, M., Rojo, T., Carriazo, D., 2019. Flat-shaped carbon-graphene microcomposites as electrodes for high energy supercapacitors. *J. Mater. Chem. A* 7, 14646–14655. <https://doi.org/10.1039/C9TA03295A>.
- Muthi Aturoifah, N.I., Diantoro, M., Meevasana, W., Maensiri, S., 2024. Enhancing supercapacitor performance with cassava tuber- bamboo stem blended porous activated carbon: an environmentally friendly approach. *E3S Web Conf.* 517, 10003. <https://doi.org/10.1051/e3sconf/202451710003>.
- Muthurasu, A., Ganesh, V., 2012. Electrochemical characterization of Self-assembled Monolayers (SAMs) of silanes on indium tin oxide (ITO) electrodes - Tuning electron transfer behaviour across electrode-electrolyte interface. *J. Colloid Interface Sci.* 374, 241–249. <https://doi.org/10.1016/j.jcis.2012.02.007>.
- Omokafe, M.S., 2020. Fabrication of Activated Carbon from Coconut Shells and its Electrochemical Properties for Supercapacitors. *Int. J. Electrochem. Sci.* 10854–10865. <https://doi.org/10.20964/2020.11.10>.
- Ospino Orozco, J., Parra Barraza, J., Cervera Cahuana, S., Coral Escobar, E.E., Vargas Ceballos, O., 2022. Activated carbon from cassava peel: A promising electrode material for supercapacitors. *Rev. Fac. Ing. Univ. Antioquia* 102, 88–95. <https://doi.org/10.17533/udea.redin.20200803>.
- Owusu, K.A., Wang, Z., Qu, L., Liu, Z., Mehrez, J.-A.-A., Wei, Q., Zhou, L., Mai, L., 2020. Activated carbon clothes for wide-voltage high-energy-density aqueous symmetric supercapacitors. *Chinese Chem. Lett.* 31, 1620–1624. <https://doi.org/10.1016/j.ccl.2019.09.045>.
- Peng, C., Lang, J., Xu, S., Wang, X., 2014. Oxygen-enriched activated carbons from pomelo peel in high energy density supercapacitors. *RSC Adv.* 4, 54662–54667. <https://doi.org/10.1039/C4RA09395J>.
- Phainuphong, S., Taweekun, J., Maliwan, K., Theppaya, T., Reza, Md. Sumon, Azad, A. K., 2022. Synthesis and characterization of activated carbon derived from rubberwood sawdust via carbonization and chemical activation as electrode material for supercapacitor. *J. Adv. Res. Fluid Mech. Therm. Sci.* 94, 61–76. <https://doi.org/10.37934/arfmts.94.2.6176>.
- Pramitha, A., Hegde, S.S., Bhat, B.R., George, S.D., Sudhakar, Y.N., Raviprakash, Y., 2023. Properties of Mn₃O₄ thin film electrodes prepared using spray pyrolysis for supercapacitor application. *Mater. Chem. Phys.* 307, 128213. <https://doi.org/10.1016/j.matchemphys.2023.128213>.
- Pramitha, A., Hegde, S.S., Bhat, B.R., Yadav, C., Chakraborty, S., Ravikumar, A., George, S.D., Sudhakar, Y.N., Raviprakash, Y., 2024. Unveiling the mass-loading effect on the electrochemical performance of Mn₃O₄ thin film electrodes: a combined computational and experimental study. *Phys. Scr.* 99, 105922. <https://doi.org/10.1088/1402-4896/ad7206>.
- Qian, W., Sun, F., Xu, Y., Qiu, L., Liu, C., Wang, S., Yan, F., 2014. Human hair-derived carbon flakes for electrochemical supercapacitors. *Energy Environ. Sci.* 7, 379–386. <https://doi.org/10.1039/C3EE43111H>.
- Rawal, S., Joshi, B., Kumar, Y., 2018. Synthesis and characterization of activated carbon from the biomass of Saccharum bengalense for electrochemical supercapacitors. *J. Energy Storage* 20, 418–426. <https://doi.org/10.1016/j.est.2018.10.009>.

- Sahoo, M.K., Rao, G.R., 2021. A high energy flexible symmetric supercapacitor fabricated using N-doped activated carbon derived from palm flowers. *Nanoscale Adv.* 3, 5417–5429. <https://doi.org/10.1039/D1NA00261A>.
- Saputro, E.A., Wulan, V.D.R., Winata, B.Y., Yogaswara, R.R., Erliyanti, N.K., 2020. Process of Activated Carbon from Coconut Shells Through Chemical Activation. *Nat. Sci. J. Sci. Technol.* 9. <https://doi.org/10.22487/25411969.2020.v9.i1.15042>.
- Selvaraj, A.R., Kim, H.-J., Senthil, K., Prabakar, K., 2020. Cation intercalated one-dimensional manganese hydroxide nanorods and hierarchical mesoporous activated carbon nanosheets with ultrahigh capacitance retention asymmetric supercapacitors. *J. Colloid Interface Sci.* 566, 485–494. <https://doi.org/10.1016/j.jcis.2020.01.117>.
- Shahrokhian, S., Rahimi, S., Mohammadi, R., 2018. Nickel-cobalt layered double hydroxide ultrathin nanosheets coated on reduced graphene oxide nanosheets/nickel foam for high performance asymmetric supercapacitors. *Int. J. Hydrogen Energy* 43, 2256–2267. <https://doi.org/10.1016/j.ijhydene.2017.12.019>.
- Shrestha, D., 2022. Activated carbon and its hybrid composites with manganese (IV) oxide as effectual electrode materials for high performance supercapacitor. *Arab. J. Chem.* 15, 103946. <https://doi.org/10.1016/j.arabjc.2022.103946>.
- Shrestha, D., Rajbhandari, A., 2021. The effects of different activating agents on the physical and electrochemical properties of activated carbon electrodes fabricated from wood-dust of *Shorea robusta*. *Heliyon* 7. <https://doi.org/10.1016/j.heliyon.2021.e07917>.
- Song, B., Wu, F., Zhu, Y., Hou, Z., Moon, K., Wong, C.-P., 2018. Effect of polymer binders on graphene-based free-standing electrodes for supercapacitors. *Electrochim. Acta* 267, 213–221. <https://doi.org/10.1016/j.electacta.2018.02.072>.
- Subraya Hegde, S., Ramachandra Bhat, B., 2024. Impact of electrolyte concentration on electrochemical performance of Cocos nucifera Waste-Derived High-Surface carbon for green energy storage. *Fuel* 371, 131999. <https://doi.org/10.1016/j.fuel.2024.131999>.
- Sudhan, N., Subramani, K., Karnan, M., Ilyaraja, N., Sathish, M., 2017. Biomass-derived activated porous carbon from rice straw for a high-energy symmetric supercapacitor in aqueous and non-aqueous electrolytes. *Energy Fuel* 31, 977–985. <https://doi.org/10.1021/acs.energyfuels.6b01829>.
- Taer, E., Iwantono, L., Manik, S.T., Taslim, R., Dahlan, D., Deraman, M., 2014. Preparation of activated carbon monolith electrodes from sugarcane bagasse by physical and physical-chemical activation process for supercapacitor application. *Adv. Mater. Res.* 896, 179–182. <https://doi.org/10.4028/www.scientific.net/AMR.896.179>.
- Thirumal, V., Yuvakkumar, R., Ravi, G., Dineshkumar, G., Ganesan, M., Alotaibi, S.H., Velauthapillai, D., 2022. Characterization of activated biomass carbon from tea leaf for supercapacitor applications. *Chemosphere* 291, 132931. <https://doi.org/10.1016/j.chemosphere.2021.132931>.
- Thongpat, W., Taweekun, J., Maliwan, K., 2021. Synthesis and characterization of microporous activated carbon from rubberwood by chemical activation with KOH. *Carbon Lett.* 31, 1079–1088. <https://doi.org/10.1007/s42823-020-00224-z>.
- Tran, H.N., Lee, C.-K., Nguyen, T.V., Chao, H.-P., 2018. Saccharide-derived microporous spherical biochar prepared from hydrothermal carbonization and different pyrolysis temperatures: synthesis, characterization, and application in water treatment. *Environ. Technol.* 39, 2747–2760. <https://doi.org/10.1080/09593330.2017.1365941>.
- Usha Rani, M., Nanaji, K., Rao, T.N., Deshpande, A.S., 2020. Corn husk derived activated carbon with enhanced electrochemical performance for high-voltage supercapacitors. *J. Power Sources* 471, 228387. <https://doi.org/10.1016/j.jpowsour.2020.228387>.
- Vinayagam, M., Suresh Babu, R., Sivasamy, A., Ferreira de Barros, A.L., 2020. Biomass-derived porous activated carbon from *Syzygium cumini* fruit shells and *Chrysopogon zizanioides* roots for high-energy density symmetric supercapacitors. *Biomass Bioenergy* 143, 105838. <https://doi.org/10.1016/j.biombioe.2020.105838>.
- Vinayagam, M., Suresh Babu, R., Sivasamy, A., de Barros, A.L.F., 2021. Biomass-derived porous activated carbon nanofibers from *Sapindus trifoliatus* nut shells for high-performance symmetric supercapacitor applications. *Carbon Lett.* 31, 1133–1143. <https://doi.org/10.1007/s42823-021-00235-4>.
- Vinayagam, M., Babu, R.S., Sivasamy, A., de Barros, A.L.F., 2024a. Impact of carbon dioxide-assisted activation on *Milletia pinnata* shell-derived porous activated carbon for enhanced performance in symmetric supercapacitors. *Ionics (kiel)* 30, 3045–3054. <https://doi.org/10.1007/s11581-024-05491-8>.
- Vinayagam, M., Suresh Babu, R., Sivasamy, A., de Barros, A.L.F., 2024b. Physical activation assisted porous activated carbon from *Strychnos Potatorum* shells for high-performance symmetric supercapacitors. *Mater. Lett.* 371, 136961. <https://doi.org/10.1016/j.matlet.2024.136961>.
- Wang, B., Li, L., Zhao, C., Zhao, C., 2021a. Microporous active carbon with ultrahigh surface area from *Metaplexis japonica* for high-performance supercapacitor. *Diam. Relat. Mater.* 118, 108484. <https://doi.org/10.1016/j.diamond.2021.108484>.
- Wang, R., Li, Y., Shuai, X., Liang, R., Chen, J., Liu, C., 2021b. Pectin/Activated Carbon-Based Porous Microsphere for Pb²⁺ Adsorption: Characterization and Adsorption Behaviour. *Polymers (basel)* 13, 2453. <https://doi.org/10.3390/polym13152453>.
- Wang, Q., Qin, B., Li, H.-X., Zhang, X.-H., Tian, X., Jin, L., Cao, Q., 2020. Honeycomb-like carbon with tunable pore size from bio-oil for supercapacitor. *Microporous Mesoporous Mater.* 309, 110551. <https://doi.org/10.1016/j.micromeso.2020.110551>.
- Wang, H., Xu, Z., Kohandehghan, A., Li, Z., Cui, K., Tan, X., Stephenson, T.J., King'ondo, C.K., Holt, C.M.B., Olsen, B.C., Tak, J.K., Harfield, D., Anyia, A.O., Mitlin, D., 2013. Interconnected Carbon Nanosheets Derived from Hemp for Ultrafast Supercapacitors with High Energy. *ACS Nano* 7, 5131–5141. <https://doi.org/10.1021/nn400731g>.
- Wei, H., Wang, H., Li, A., Li, H., Cui, D., Dong, M., Guo, Z., 2020. Advanced porous hierarchical activated carbon derived from agricultural wastes toward high performance supercapacitors. *J. Alloys Compd.* 820, 153111.
- Wijaya, D.R.P., Martono, Y., Riyanto, C.A., 2018. Synthesis and Characterization of Nano Activated Carbon Tea Waste (*Camellia sinensis* L.) Viewed from the Content and Ratio of Orthophosphoric Acid. *Indones. J. Chem. Res.* 3, 49–58.
- Wu, C., Liu, J., Wu, W., Wang, Y., Zhao, Y., Li, G., Zhang, Y., Zhang, G., 2025. Mild modification of sponge-like carbon: Ammonia post-treatment for enhanced CO₂ adsorption and suitability for supercapacitors. *Sep. Purif. Technol.* 353, 128525. <https://doi.org/10.1016/j.seppur.2024.128525>.
- Yadav, R.M., Li, Z., Zhang, T., Sahin, O., Roy, S., Gao, G., Guo, H., Vajtai, R., Wang, L., Ajayan, P.M., Wu, J., 2022. Amine-Functionalized Carbon Nanodot Electrocatalysts Converting Carbon Dioxide to Methane. *Adv. Mater.* 34. <https://doi.org/10.1002/adma.202105690>.
- Yang, G., Park, S.J., 2020. Nanoflower-like NiCo₂O₄ grown on biomass carbon coated nickel foam for asymmetric supercapacitor. *J. Alloys Compd.* 835, 155–270. <https://doi.org/10.1016/j.jallcom.2020.155270>.
- Yang, H., Sun, X., Zhu, H., Yu, Y., Zhu, Q., Fu, Z., Ta, S., Wang, L., Zhu, H., Zhang, Q., 2020. Nano-porous carbon materials derived from different biomasses for high performance supercapacitors. *Ceram. Int.* 46, 5811–5820. <https://doi.org/10.1016/j.ceramint.2019.11.031>.
- Yin, Y., Yin, J., Zhang, W., Tian, H., Hu, Z., Ruan, M., Song, Z., Liu, L., 2018. Effect of char structure evolution during pyrolysis on combustion characteristics and kinetics of waste biomass. *J. Energy Resour. Technol.* 140. <https://doi.org/10.1115/1.4039445>.
- Young, C., Chen, H.-T., Guo, S.-Z., 2022. Highly Porous Holey Carbon for High Areal Energy Density Solid-State Supercapacitor Application. *Micromachines* 13, 916. <https://doi.org/10.3390/mi13060916>.
- Yuli, Y., Eka, S., Yazmendra, R., 2021. Biomass waste of cocoa skin for basic activated carbon as source of eco-friendly energy storage. *J. Phys. Conf. Ser.* 1788. <https://doi.org/10.1088/1742-6596/1788/1/012020>.
- Yumak, T., Bragg, D., Sabolsky, E.M., 2019. Effect of synthesis methods on the surface and electrochemical characteristics of metal oxide/activated carbon composites for supercapacitor applications. *Appl. Surf. Sci.* 469, 983–993. <https://doi.org/10.1016/j.apsusc.2018.09.079>.
- Zapata Benabith, Z., Carrasco Marín, F., Moreno Castilla, C., 2013. Electrochemical performance of Cu- and Ag-doped carbon aerogels. *Mater. Chem. Phys.* 138, 870–876. <https://doi.org/10.1016/j.matchemphys.2012.12.076>.
- Zeigler, D.F., Candelaria, S.L., Mazzi, K.A., Martin, T.R., Uchaker, E., Suraru, S.L., Kang, L.J., Cao, G., Luscombe, C.K., 2015. N-Type Hyperbranched Polymers for Supercapacitor Cathodes with Variable Porosity and Excellent Electrochemical Stability. *Macromolecules* 48, 5196–5203. <https://doi.org/10.1021/acs.macromol.5b01070>.
- Zelinsky, S.O., Stryzhakova, N.G., Gozhenko, O.V., Maletin, Y.A., 2022. How the Electrochemical Impedance Spectroscopy Can Deepen the Understanding of Supercapacitor Performance. *Him. Fiz. Ta Tehnol. Poverhni* 13, 70–81. <https://doi.org/10.15407/HFTP13.01.070>.
- Zhang, Y., Duan, Z., Zou, H., Ma, M., 2018. Fabrication of electrospun LaFeO₃ nanotubes via annealing technique for fast ethanol detection. *Mater. Lett.* 215, 58–61. <https://doi.org/10.1016/J.MATLET.2017.12.062>.